学 位 論 文

# Theoretical Light Curves for Type Ia Supernovae

# Ia型超新星の光度曲線モデル

平成8年12月博士(理学)申請

東京大学大学院理学系研究科

天文学専攻

岩 本 弘 一

# Theoretical Light Curves for Type Ia Supernovae

A dissertation submitted in partial fulfillment of

the requirements for the degree of

Doctor of Philosophy

in

Astronomy

Koichi Iwamoto

Department of Astronomy, School of Science,

University of Tokyo

December 1996

# Abstract

A new radiation hydrodynamics code has been developed to calculate more sophisticated theoretical light curves and spectra of supernovae(SNe) to be confronted with high quality data by recent photometric and spectroscopic observations. The frequency integrated moment equations of radiative transfer are solved with the Eddington factors which are obtained by simultaneously solving the time-dependent multi-frequency and multi-angle radiative transfer equation. The $O(v/c)$ terms both in the moment equations and the transfer equation are consistently retained to ensure the correct solutions in a rapidly expanding supernova ejecta.

With the new code, the bolometric and the *UBVRI* light curves of the Chandrasekhar mass white dwarf models for Type Ia supernovae are calculated. The models applied here cover a standard deflagration model W7 and a series of delayed detonation models with a parameterized transition density from deflagration to detonation. The light curve properties such as the rising time, the peak luminosity and the decline rate are carefully examined for each model and compared to those of the published photometries of normal SNe Ia 1937C, 1972E, 1981B, 1989B, and 1994D and the peculiar SN 1991T, an extreme case of over-luminous events.

The model dependence of the light curve properties are derived from the above set of the theoretical model calculations. We discuss some general trend of the light curve shape that could discriminate the Chandrasekhar mass and the sub-Chandrasekhar mass explosions. The interesting features of the observed light curves such as an intrinsic spread of the peak absolute magnitude and the brighter-slower relation between the maximum brightness and the decline rate, $M_{\rm max}$ versus $\Delta m_{15}(B)$, are discussed from a theoretical point of view. The influences of the input atomic physics and the adopted numerical techniques are also discussed.

Finally, a tentative estimate of the Hubble constant $H_0$ is given based on the above comparisons between the theoretical light curves and the observations. The light curve fitting in the multi-color bands allows for the determinations of the interstellar extinctions and the distances to the parent galaxies independently of the other distance indicators, which could be an interesting alternative method to the other empirical ones based on the hypothesis of the homogeneity of SNe Ia or the approximate luminosity-decline rate relation. As a result of fitting for the above sample of SNe Ia, we find the value of the Hubble constant to be $H_0 = 66 \pm 12$ km sec$^{-1}$ Mpc$^{-1}$.

# Contents

Abstract

**1 Type Ia Supernovae** **1**

1.1 Introduction . . . . . 1

1.2 Observational Overview . . . . . 3

1.3 Evolutionary Scenarios of Progenitor Systems . . . . . 4

1.4 Theoretical Light Curve Modeling . . . . . 6

**2 Hydrodynamical Models and Nucleosynthesis** **11**

2.1 Chandrasekhar vs. sub-Chandrasekhar Mass . . . . . 12

2.2 Chandrasekhar Mass Models . . . . . 13

2.2.1 Deflagration Models . . . . . 13

2.2.2 Late Detonation Models . . . . . 14

2.2.3 Delayed Detonation Models . . . . . 14

**3 The Equations of Radiative Transfer** **25**

3.1 The Boltzman equation for photons . . . . . 25

3.2 The Transfer Equation in the Comoving Frame . . . . . 27

3.3 Moments of the Transfer Equation . . . . . 29

3.4 Radiation Hydrodynamics . . . . . 31

**4 Preliminary Inquiries with Grey Opacities** **35**

4.1 Light Curve Analysis with Simple Models . . . . . 35

4.2 Test Problem with Grey Opacities . . . . . 37

**5 Light Curve Modeling with Realistic Opacities** **41**

5.1 Opacity . . . . . 41

5.2 Equation of State and Gamma Ray Deposition . . . . . 44

5.3 Predicted Light Curves and Spectra . . . . . 46

5.4 Correlation between Luminosity and Light Curve Shape . . . . . 49
5.5 Comparisons with Observations . . . . . 54
5.6 Comparative Distance Determinations . . . . . 56
5.7 Expansion Effect on Line Opacity . . . . . 63

**6 Determinations of Cosmological Parameters** **65**
6.1 Overview . . . . . 65
6.2 Hubble Constant . . . . . 66

**7 Conclusions** **75**

**A Numerical Methods** **81**
A.1 Radiative Transfer . . . . . 81
A.2 Radiation Hydrodynamics . . . . . 81

# Chapter 1

# Type Ia Supernovae

## 1.1 Introduction

Supernova is such a magnificent event in the celestial sphere that suddenly appears in a point of the sky and begins to shine as bright as its parent galaxy. It is the result of the explosion of evolved stars when they come to the end of their life. It releases vast amount of energy $\sim 10^{53}$ erg, most of them is carried away by neutrinos with little interaction with matter. Only a small fraction of the liberated energy ($\sim 1\%$) is converted to kinetic energy of ejected gas and further smaller part of it is radiated as photons. It is said that the first discovery of supernovae may go back to ancient China or Orient. The supernova studies in modern astronomy had begun in 1930's after the pioneering work by Baade & Zwicky.

Supernovae(SNe) are classified observationally as type I or type II based on their spectroscopic features in the optical light. Type II supernovae(SNe II) show hydrogen lines while Type I supernovae(SNe I) do not. SNe I are further divided into three subclasses of Ia, Ib and Ic. SNe Ia are characterized by strong SiII absorption lines at their maximum light while SNe Ib and Ic being lacking in them. It is generally believed now that SNe Ia correspond to the thermonuclear supernovae whereas SNe Ib and Ic originate from the core-collapse supernovae as SNe II do. There are many additional characteristics that discriminate these subclasses one another and from other types of supernovae(Wheeler 1990; Filippenko *et al.*1986). The progress of observational techniques and an increasing amount of data accumulated during the past decades have made supernovae classification more complicated. Even a new category, 'Type IIb', has been added for a recent peculiar supernova SN 1993J(Nomoto *et al.*1993; Podsiadlowski *et al.*1993).

It is prevalently accepted that a Type Ia supernova is produced by the thermonuclear explosion of an accreting white dwarf in a close binary system. Theoretically, it is likely that the ignition of the nuclear burnings takes place near the Chandrasekhar mass $\sim 1.4\ M_{\odot}$, which is the upper

limit of the mass which electron degenerate cold stars can have. This is consistent with the apparent homogeneity of SNe Ia and their occurrence in all types of galaxies. But, the recent discoveries of sub-luminous SNe Ia have prompted the idea of the explosion of sub-Chandrasekhar mass white dwarfs. After the advent of exceptionally over-luminous event SN 1991T, the situation has become more open to various explosion models. Theoretically, the realization frequency of possible evolutionary scenarios in close binaries has been investigated to select promising candidate systems for SNe Ia progenitors(Iben & Tutukov 1984; Ruiz-Lapuente *et al.*1995; Canal *et al.*1996), which include an interesting possibility that the explosion is triggered by the coalescence of two white dwarfs with a total mass exceeding the Chandrasekhar limit(double degenerate scenario, Iben & Tutukov 1984) However, the detail of mass transfer process in close binary systems has long been a highly uncertain issue. It is true, in particular, of the common envelope phase which could occur in the non-conservative mass transfer in binaries with very different masses.

SNe Ia have a large impact on the chemical evolution of the galaxies(Tsujimoto etal. 1995; Renzini et al. 1993). SNe Ia are the main contributors to the iron yield according to the calculations of explosive nucleosynthesis in supernova ejecta. As the progenitor of SN Ia are low-mass stars with relatively long lifetime, iron could be a useful element as a clock to look back the history of the galaxy formation. The analysis of the abundance ratios of solar neighborhood stars, with the aid of the galactic chemical evolution model, suggests the mean lifetime of the progenitors of SN Ia $\sim 1.5$ Gy (Yoshii et al. 1996) On the other hand, an increasing number of evidences for the observational diversity among SNe Ia imply that SNe Ia can be produced by different stellar populations with a wide range of ages and metallicities. In this respect, it is particularly important to understand the evolutionary scenarios of the progenitor system of SNe Ia.

As well as several important aspects of SNe Ia mentioned above, one of the most significant application of them has been made to the problem of determining the cosmological parameters. The large luminosity of supernova allows for its use to measure the extragalactic distances and to determine the Hubble constant $H_0$. Both SNe I and SNe II can be and have been used so far to do this, however, SNe Ia have been regarded more promising one because they are brighter ($\sim 2$ magnitude) and more often detected in magnitude limited surveys(Hamuy *et al.*1996). Although SNe Ia are not considered as perfect standard candles now, they still remain to be good distance indicators because their peak luminosity well correlate with the decline rate of the light curves. Recently, Höflich & Khokhlov(1996) fitted their state of the art theoretical light curves to the individual observations of SNe Ia and obtained the value of $H_0 = 67 \pm 9$ km sec$^{-1}$ Mpc$^{-1}$. Their method relies only on the theoretical light curves and does not depend on any other astronomical calibrations. The details of this method will be discussed later, where we give a tentative estimate of $H_0$ based on our own theoretical light curves.



## 1.2 Observational Overview

The most striking characteristic of SNe Ia is that they have shown quite similar light curves and spectra except for some peculiar events (see reviews by Branch et al.1995, Filleppenko 1996). The similarity of the light curve shapes was first pointed out by Pskovskii(1967) and Kowal(1968). Recently, Leibundgut et al.(1991) constructed the templates for the optical light and color curves from the photometric data of 75 SNe Ia and clearly showed that most SNe Ia in their sample comply with the templates within the observational errors. The peak absolute magnitudes of normal SNe Ia are found to be $M_B \simeq M_V \simeq -19.75 + 5\log(H_0/50 \text{ km s}^{-1}\text{Mpc}^{-1})$ with the intrinsic dispersion less than $\sigma(M_B) \simeq \sigma(M_V) \simeq 0.2$(Branch et al. 1996). Most SNe Ia in the observational sample are not strongly extinguished by dust in their parent galaxies and have a well-defined color evolution, with $B-V$ reddening from near 0.0 at maximum light to near 1.0 a month later(Branch et al.) Figure 1.1 shows the $B, V$ and $U$ light curves and $B-V, U-B$ color evolutions of a well-observed SN 1981B with the template curves(Figure 68 in Leibundgut et al. 1991).

The spectra of SNe Ia are characterized by a deep absorption trough near 6150 Å, interpreted as blueshifted SiII $\lambda\lambda$ 6347, 6371, which is absent in SNe Ib and Ic. SNe Ib have instead prominent lines of HeI, while SNe Ic show neither of them. The spectra of SNe Ia near the maximum light are dominated by lines of singly ionized or neutral species like SiII, CaII, SII, and OI with a velocity ranging from 8,000 to 30,000 km s$^{-1}$. This indicates that fast expanding outer layers of the ejecta are mainly composed of intermediate-mass elements from O to Ca (Branch et al. 1983). At later phase, the spectral feature changes to the nebular one abundant in the lines of the iron-peak elements. All SNe Ia show a strong UV deficit relative to the blackbody fit at optical wavelengths(Panagia 1987) because of the line blanketing effects by numbers of transitions mostly due to FeII and CoII (Branch & Venkatakrishna 1986). The $I$ and $R$ bands light curves of SNe Ia tend to be very flat and generally show the secondary peak a month later the maximum light. Figure 1.2 shows the spectra of normal and peculiar SNe Ia at the maximum light (Fig.1 and Fig.2 in Branch et al. 1993).

Although the majority of SNe Ia in the observational sample have shown quite homogeneous characteristics as stated above, some SNe Ia have revealed their conspicuous peculiarities(Branch et al 1993). For example, SN 1991bg(Fillipenko et al. 1992; Leibundgut et al. 1993), 1992K(Hamyu et al. 1994), and 1986G(Phillips et al. 1987; Cristiani et al. 1992), have dimmer and faster light curves than the normal SNe Ia. Their spectra indicate lower expansion velocities, lower extinction, and redder colors compared with typical SNe Ia. An event at the opposite end of the variations is, for example, SN 1991T(Filippenko et al. 1992; Phillips et al. 1992;

Ruiz-Lapuente et al. 1992), whose early spectra lacked the intermediate-mass elements in the outermost layers(Jeffery et al. 1992) and light curves was much brighter and somewhat slower than the normal SNe Ia(Phillips 1993).

The correlations between the decline rate and other properties of SNe Ia light curves has long been recognized since the analysis by Barbon et al.(1973) and Pskovskii (1977,1984). Branch(1981) studied the correlations between the expansion velocity, the peak absolute magnitude and the post-maximum decline rate of the light curves. However, small size of their sample in elliptical galaxies and possible contamination from SNeIb/Ic in spirals raised some doubt on its statistical significance. Recently, Phillips(1993) carefully analyzed a sample of nine well-observed SNe Ia and confirmed a tight correlation between the decline rate of the $B$ light curve and the absolute magnitudes or the intrinsic colors at maximum light (Figure 1.3, Phillips 1993 ). He introduced a measure $\Delta m_{15}(B)$, which is the total amount that $B$ light curve drops during the first 15 days after its maximum. With the luminosity-decline rate correlation taken into account, Hamuy et al.(1996) obtained a Hubble diagram with less dispersion for the sample discovered by the recent Calán/Tololo supernova survey. This fact implies the existence of a continuous sequence of the progenitor masses or the diversity of the explosion mechanism. It is important to clarify the physical origin of the correlations through theoretical light curve modeling.

## 1.3 Evolutionary Scenarios of Progenitor Systems

Although the exploding C+O white dwarfs are widely accepted as plausible models for SNe Ia, their presupernova evolution in close binary systems, the scenarios that could actually produce SNe Ia, has not yet been well understood. In terms of triggering mechanism of the explosion, there have been proposed two major distinct scenarios. One is the accreting white dwarf scenario in which the accretion of matter from the companion star on the top of white dwarf surface will activate the cooling white dwarf, ultimately bringing them to the ignition condition. The other one involves the coalescence of a pair of the degenerate white dwarfs that have reduced the orbital separation by losing their angular momentum due to the gravitational wave radiation(double degenerate scenario, Iben & Tutukov 1984; Tutukov & Yungelson 1994).

The evolution of accreting white dwarfs in the former scenario has been extensively studied by Nomoto(1982a,1982b), Iben et al.(1987), and Nomoto & Kondo(1991). The accumulated materials on the C+O core compresse the white dwarf increasing the interior densities and raising the temperatures due to adiabatic compression. At the same time, the released gravitational energy causes a significant temperature rise near the surface. The final fate of accreting white dwarfs mainly depends on the accretion rate $\dot{M}$ since whether the white dwarf can grow its mass or



not is determined by the strength of hydrogen/helium shell flashes near the surface. (Nomoto 1982a; Nomoto & Kondo 1991). The resulting outcome is summarized as follows(Nomoto 1982ab; Nomoto et al. 1984; Nomoto & Kondo 1991).

For sufficiently massive and cool white dwarf, the central region is compressed only adiabatically, therefore it remains cold when carbon is ignited in the center at densities as high as $10^{10}$ g cm$^{-3}$ and an accretion-induced collapse(AIC) will be the outcome(Nomoto & Kondo 1991). For smaller initial white dwarf mass $M_{\rm C+O} < 1.2 M_\odot$, heat inflow from the surface layer ignites carbon at relatively low central density ($\rho \sim 3 \times 10^9$ g cm$^{-3}$), which makes a successful explosion of SN Ia.

1. For relatively fast accretion with $\dot{M} \approx 10^{-8} - 10^{-6} M_\odot {\rm yr}^{-1}$, the stable and steady hydrogen shell burning for below the Paczyński's(1970) critical accretion rate or relatively weak recurrent hydrogen and (or helium) shell flashes(Taam 1980; Fujimoto & Sugimoto 1982) for above the rate could be the case. In both cases, the white dwarf grows its mass to the Chandrasekhar limit before the carbon ignition and finally ends with a centrally ignited carbon deflagration supernova although the actual process of burning propagation is still uncertain.(Chandrasekhar-mass explosion)

2. For relatively slow accretion with $\dot{M}$ below $\approx 1 \times 10^{-8} M_\odot {\rm yr}^{-1}$, the helium shell flash at or near the surface is strong enough to ignite an off-center helium detonation(Nomoto 1982b; Woosely 1986,1993; Hashimoto et al. 1986). The helium detonation could induce an inwardly propagating carbon detonation(Nomoto 1982) or a central carbon detonation which is indirectly ignited by a shock wave that converges at the center(Livne 1990, Woosely & Weaver 1994). (sub-Chandrasekhar explosion)

The critical accretion rate $10^{-8} M_\odot {\rm yr}^{-1}$ that divides Chandrasekhar(Ch) and sub-Ch mass explosions will be lowered if the wind-type mass loss occurs during the accretion process. Hachisu, Kato, & Nomoto(1996ab) found a static solution for such systems by using the updated OPAL Rosseland mean opacity, which has a large enhancement around $1.6 \times 10^5$ K.

For double degenerate scenarios, Kawai, Saio, & Nomoto(1987) studied the ignition of nuclear burning in merging white dwarfs for various combinations of component stars consisting of He, C+O, and O+Ne+Mg. They simulated the merging process by employing the steady models of the massive component rapidly accreting the transferred material. For C+O white dwarf binaries, they found that off-center carbon ignition would take place at sub-Chandrasekhar masses down to $\sim 1\ M_\odot$, although the subsequent evolution after the off-center ignition depends on the accretion rate. To simulate the actual merging process in the binary system is a hard problem and has been treated mostly by simple analytic models that account for energy budget. Direct numerical simulations of common envelope evolution have been conducted by Livio & Soker(1988) and Taam

& Bodenheimer(1989), giving the mass transfer efficiency parameter "$\alpha \sim 0.3 - 0.6$".

Realization frequencies of SN Ia event in various types of binary systems have been estimated to distinguish plausible scenario (Iben & Tutukov 1984; Ruiz-Lapuente et al. 1995; Canal et al. 1996; Tutukov & Yungelson 1994; Branch et al. 1995). There are still large uncertainties in the detailed processes of mass transfer or common envelope evolution and any conclusions are suffered from the ambiguous factors such as mass transfer rate, mass transfer efficiency. At the present stage, we could consider all scenarios might partially contribute to the observed SNe Ia.

There have been discussions on observational diagnostics for the evolutionary origins of the progenitor systems. Possible association of the progenitor system of SNe Ia with the super-soft X-ray sources(SSXS) has been argued by van den Heuvel *et al.*(1992), Rappaport *et al.*(1994), or Iben & Tutukov(1995). Livio(1995) pointed out that SSXSs should have stellar wind-type mass loss and possibly also additional mass loss associated with helium shell burning on the white dwarf surface. Their column density to ionizing radiation could be as significant as to produce a compact circumstellar ionized region.

Such circumstellar nebulae that will be swept up by supernova ejecta might be detected soon after the explosion. Lundqvist & Cumming (1996) predicted the possible $H_\alpha$ luminosities and the nature of X-ray emissions for various wind-type mass loss rates. They obtained a constraint $\dot{M} \leq 2.5 \times 10^{-5} M_\odot \mathrm{yr}^{-1}$ for SN Ia 1994D with the observed H$\alpha$ luminosity. In the symbiotic star scenario(e.g.,Munari & Renzini 1992), a substantial CSM is to be expected. The detectability of radio emissions from the circumstellar material (CSM) around SN Ia was studied by Boffi & Branch(1995). Branch et al. (1996) discussed the upper limit(Eck et al. 1995) to the radio flux from 1986G in NGC 5128(Cen A), a week before optical maximum, indicates the lack of a dense CSM and that the progenitor of SN 1986G was not a symbiotic system, though SN 1986G was a peculiar weak SN Ia. They also studied SN 1981B, another SN Ia whose radio upper limit had been obtained(Sramek & Weiler 1990) and found it marginally inconsistent with the predictions for a mass-loss rate expected in symbiotic systems.

## 1.4 Theoretical Light Curve Modeling

The recent observations have revealed that SNe Ia can no longer be considered "standard candles" and they rather show some extent of diversities in the peak absolute magnitude and in the light curve shape. In addition, it has been noticed that there seems to exist some correlations between the luminosity and the light curve shape of SNe Ia(Phillipse 1993; Hamuy et al. 1995, 1996). It is a primarily important question for theories of Type Ia supernovae whether such dispersions in light curve properties and the correlation could be explained within the Chandrasekhar mass models or



we need to introduce the sub-Chandrasekhar mass models. When we use SNe Ia to determine the Hubble constant, it is an essential issue whether the origin of the observed dispersion is the scatter in the interstellar extinctions or the intrinsic variations among SNe Ia explosions. As a first step to clarify these problems, we restrict our investigation to the Chandrasekhar mass models and examine how the light curve properties depend on the explosion models.

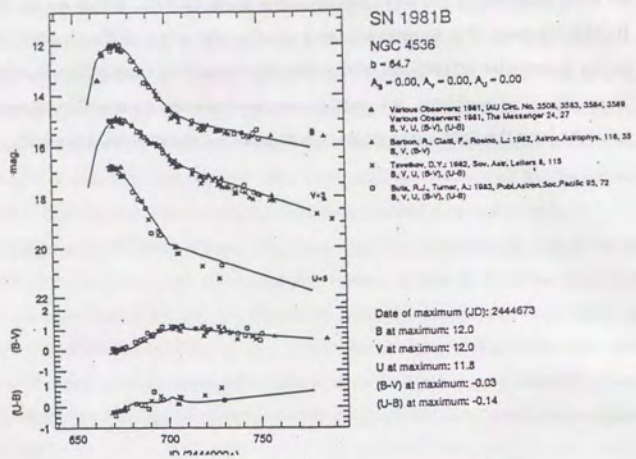


Figure 1.1: $U, B, V$ light curves and $B-V, U-B$ color evolutions of SN 1981B with template curves(Leibundgut *et al.*1991)

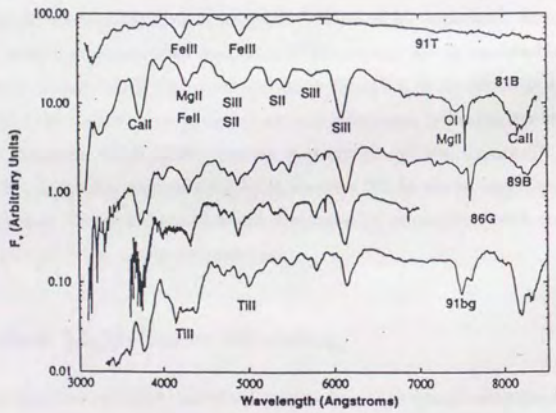


Figure 1.2: The spectra of SNe Ia near maximum light. Included are two normal SNe Ia(SN 1981B: Branch *et al.*1983; SN 1989B: Wells *et al.*1993) and three peculiar SNe Ia(SN 1991T: Filippenko *et al.*1992a; SN 1986G: Cristiani *et al.*1992; SN 1991bg; Filippenko et al. 1992b)



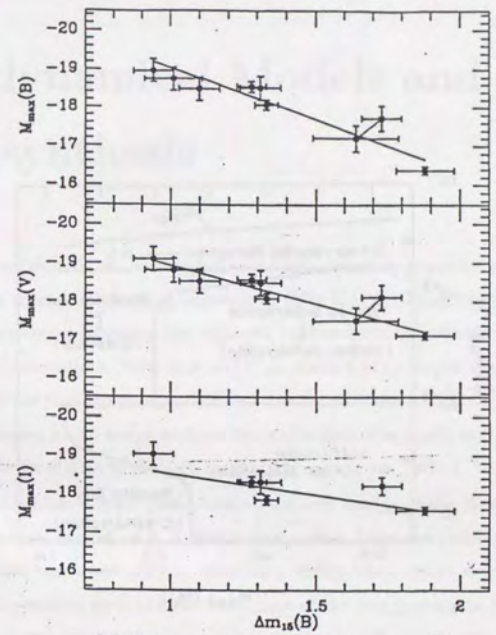


Figure 1.3: Decline rate-peak luminosity relation for the nine well-observed SNe Ia. Absolute magnitudes in $B, V$, and $I$ are plotted against $\Delta m_{15}(B)$, which measures the amount in magnitudes that the $B$ light curve drops during the first 15 days following maximum. (Phillips(1993)

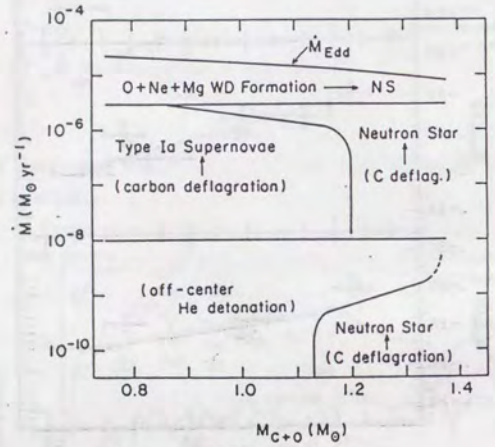


Figure 1.4: The final fate of accreting C+O white dwarfs on the plane of initial mass $M_{C+O}$ versus accretion rate $\dot{M}$ (Nomoto & Kondo 1991).

# Chapter 2

# Hydrodynamical Models and Nucleosynthesis

Thermonuclear explosion of an accreting C+O white dwarf is generally believed to be one of the most plausible models for Type Ia supernovae (SNe Ia). A Chandrasekhar-mass white dwarf undergoes total disruption following the explosive nuclear burning initiated at central part of the white dwarf. The observational facts such as (1) an absence of hydrogen in their spectra, (2) high expansion velocities of photospheres, and (3) apparent uniformity of SNe Ia, strongly support this scenario. Furthermore, it can easily explain the production of as much as 0.5 $M_\odot$ $^{56}$Ni needed to power the light curves of SNe Ia through radioactive decays via $^{56}\mathrm{Ni} \rightarrow {}^{56}\mathrm{Co} \rightarrow {}^{56}\mathrm{Fe}$ .

From the conservation laws of mass, momentum and energy of the fluid, two distinct modes of burning propagation are derived. A detonation occurs if the compressional heating is strong enough to ignite the unburned matter, whereas a deflagration moves due to the thermal conduction. Simple detonation models make most part of the star burnt into iron-peaked elements. On the other hand, the deflagration propagates slowly at quite a subsonic speed and leaves the intermediate mass elements like O, Mg, Si, and Ca, which are required from the presence of strong lines of these elements in the spectra of SNe Ia(Branch et al. 1985).

A subsonic burning front is Rayleigh-Taylor (R-T) unstable since it forms a sharp density gradient in the opposite direction of the gravity. If the flame front is wrinkled by the instability, the increase of the surface area would enhance the flame speed effectively. A number of hydrodynamical simulations have shown that with a suitable choice of parameter for the mixing a flame has a sufficient effective velocity to produce a successful explosion for SNe Ia. (ex. Nomoto et al. 1984) This simple deflagration model can predict the light curves and spectra in excellent agreement with observations.

If the flame speed exceeds the Chapman-Jouguet velocity, it would be able to make transition to

detonation. As an alternative to the simple deflagration model, this case has also been well studied as the delayed detonation (Khokhlov 1991ab), the late detonation (Yamaoka et al. 1992), or the pulsational deflagration models (Nomoto, Sugimoto, & Neo, 1976). In this case, the deflagration is assumed to transit to detonation after it reaches a certain point in the outer part of the white dwarf. The explosive C-burning at the densities as low as $3 \times 10^7$ g cm$^{-3}$ can leave the intermediate mass elements even in the detonation mode as was found by Thielemann, Nomoto, & Yokoi(1984).

## 2.1 Chandrasekhar vs. sub-Chandrasekhar Mass

For Chandrasekhar mass white dwarf models, carbon burning in the central region leads to thermonuclear runway. At such a high central density as $\sim 3 \times 10^9$ g cm$^{-3}$, nuclear energy release is only $\sim 20$ % of the Fermi energy of degenerate electrons. Therefore, the resulting shock wave was found to be not strong enough to directly form a supersonic detonation wave (Ivanova *et al.*1975; Nomoto, Sugimoto, & Neo 1976). Afterwards flame front propagates at a subsonic speed as a deflagration wave due to heat transport across the front. Since the densities in the burned layers are smaller than the overlying unburned layers, the flame front becomes Rayleigh-Taylor unstable. Resulting mixing of unburned materials into hot region and the deformation of burning front enhances the flame speed as simulated in 1D (Nomoto *et al.*1976, 1984; Woosley & Weaver 1986ab; Woosley 1990) and 2D (Müller & Arnett 1986; Livne 1993; Arnett 1994) calculations. Since the propagation of the deflagration wave is subsonic, the density when it encounters in the outer layer has already decreased due to the expansion of the white dwarf.

In the outer layers a relatively fast deflagration induces a formation of a detonation wave. For example, the carbon deflagration model C8, whose propagation velocity $v_{\rm def}$ is slightly higher than W7, has a precursor shock which is strong enough to induce a detonation in the outer layers (Nomoto *et al.*1984; model F7 in Woosley & Weaver 1986a; delayed detonation models in Khokhlov 1991a). The transition from deflagration to detonation can occur when the flame speed $v_{\rm def}$ is accelerated to the Chapman-Jouguet velocity $v_{\rm CJ}$. The transition is more likely to occur at lower densities, because the ratio of the Chapman-Jouguet velocity to the sound velocity $v_{\rm CJ}/v_s$ is smaller due to a larger density jump across the flame front (Khokhlov 1991a), while $v_{\rm def}/v_s$ is larger at lower density(Nomoto *et al.*1984). Since the convictive deflagration front may well be quite turbulent and the acceleration of $v_{\rm def}$ may take place in an indeterministic manner, the condition of the transition from deflagration to detonation has not been well understood (e.g., Williams 1985) and it could occur even for $v_{\rm def} < v_{\rm CJ}$ (Khokhlov 1991a; Woosley & Weaver 1994a).

For sub-Chandrasekhar mass models, a carbon detonation may possibly be ignited by off-center helium detonation(Livne 1990; Woosley & Weaver 1994b) or by off-center carbon flashes (Shigeyama *et al.*1992). Because of low central densities, nucleosynthesis in the detonation wave produces a significant amount of intermediate mass elements. This is in contrast to the carbon detonation model where the explosive carbon burning takes place at such high densities as $\geq 10^8$ g cm$^{-3}$ and produces mostly iron-peak elements (Arnett 1969). In the helium-detonation-induced models, the off-center helium detonation produces $^{56}$Ni and He together in the high velocity outermost layers. Because of the presence of radioactive $^{56}$Ni near the surface, the spectra would be highly non-LTE. Whether the helium features excited by $\gamma$-rays appear or not would be a crucial diagnosis (Lucy 1991; Swartz *et al.*1993). Examinations of the non-LTE synthetic spectra for these models are necessary. Also, since there is no oxygen in the outermost layers, the velocity of oxygen is much less than 22,000 km s$^{-1}$(e.g., $\leq 14,000$ km s$^{-1}$in the W7DHE model; Yamaoka *et al.*1992) unless some non-spherical effects operate.



If the majority of SNe Ia originate from the sub-Chandrasekhar mass white dwarfs with possibly a wide range of masses, the question is why SNe Ia are quite uniform. Nomoto *et al.*(1996) presented a possible answer to the question. The initial mass of a white dwarf at its formation in a close binary system is likely to be $\sim 1.0\ M_\odot$ rather than $\sim 0.6\ M_\odot$ if it is formed from case BB binary evolution. In case BB, a star with an initial mass of $5 - 8\ M_\odot$ once becomes a helium star of $1.5 - 2\ M_\odot$, which greatly expands to undergo the Roche lobe overflow when its degenerate C+O core grows to $\sim 1\ M_\odot$ (e.g., Sugimoto & Nomoto 1980; Nomoto 1982c). Since the onset stage of the helium envelope expansion depends on the density contrast between the central region and the envelope, the resulting white dwarf mass ($\sim 1\ M_\odot$) is determined strongly by the electron degeneracy in the central region of the core, thereby depending only weakly on the envelope mass.

## 2.2 Chandrasekhar Mass Models

### 2.2.1 Deflagration Models

The W7 model by Nomoto *et al.*1984 is a typical example of carbon deflagration models and its nucleosynthesis prediction has been found to be in a excellent agreement with the observed spectra of normal SNe Ia. Their flame propagation is prescribed by the mixing length theory. 'W7' corresponds to a mixing length $l = 0.7H_P$, where $H_P$ is the pressure scale height, which produced a flame speed about one-fifth of the sound speed on average. Thielemann *et al.*(1986) discussed the details of explosive nucleosynthesis in W7 as a function of the density at the flame front. In the inner layer ($\rho > 210^8$ g cm$^{-3}$), materials are incinerated into iron-peak elements, mostly $^{56}$Ni , while in the outer lower density layers ($\rho \approx 5 - 10\ 10^7$ g cm$^{-3}$), the peak temperature is too low to complete silicon burning and thus only the intermediate elements Ca, Ar, S, and

Si are produced from oxygen burning. In the layers with $\approx 2 - 5\ 10^7$ g cm$^{-3}$, carbon and neon burnings synthesize S, Si, and Mg. The decaying deflagration is extinguished in the outermost layers ($\leq 1 \times 10^7$ g cm$^{-3}$), where C and O are left unburned. The composition structure after freeze-out is shown as a function of enclosed mass from the center in Figure 2.1. Synthetic spectra of W7 has been found to be in excellent agreement with the observed optical spectra of SN 1981B (Branch *et al.*1985) and 1989B (Harkness 1991). Figures 2.1 and 2.2 show the density, velocity, and composition structures of ejecta for the models W7 and W70, respectively.

### 2.2.2 Late Detonation Models

Yamaoka *et al.*(1992) presented several late detonation models (W7DN, W7DT, W7DHE) to explain the newly observed premaximum features of the peculiar SNe Ia 1990N and 1991T in a unified manner. The fast carbon deflagration like W7 and W8 produces a central Fe/Co/Ni core and an intermediate Si/S/Ca layer and later is transformed into a detonation in the outermost layers, which forms, depending on the transition density, Fe-dominated surface layers(W7DHE) or Si/Fe-rich surface layers(W7DT,W7DN). In these models, the expansion velocities of Si and S in the outer layers well exceed 20,000 km s$^{-1}$. Yamaoka(1992) showed that W7DT and W7DN can well produce the bolometric light curves of SN 1991T and SN 1990N constructed from the observations. Figures 2.3-2.5 show the density, velocity, and composition structures of ejecta for the models W7DN, W7DT, and W7DHE.

### 2.2.3 Delayed Detonation Models

The outcome of carbon deflagration depends on its flame speed, which is highly uncertain. If the flame speed is much slower than in W7, the hydrodynamical behavior would be very different. Such a slow flame model with oscillation produces too small a kinetic energy of explosion to account for SN Ia. As mentioned above, however, the deflagration might induce a detonation at low density layers. In the delayed detonation model (Khokhlov 1991a; Woosley & Weaver 1994a), the deflagration wave is assumed to be transformed into detonation at a certain layer during the first expansion phase; here a quick acceleration of the flame speed to $v_{CJ}$ or quite a turbulent frame is assumed at the transition. In the pulsating delayed detonation model (Khokhlov 1991b), the transition into detonation is assumed to occur near the maximum compression due to mixing and compression. In these models, a carbon detonation propagates through the layers with $\rho < 10^8$ g cm$^{-3}$, which is much lower than in the central carbon detonation model.

We constructed deflagration models with a parametrized transition density. The slow deflagration with a flame speed of 1.5 % the local sound speed is artificially transformed into detonation when the density ahead of the flame decreases to 3.0, 2.2, and 1.7 $\times 10^7$ g cm$^{-3}$ (WDD3, WDD2,



Table 2.1: List of the Hydrodynamical Models for SNe Ia Investigated

| Model | Mass ( $M_\odot$) | Energy ( $10^{51}$ ergs ) | $M_{^{56}\mathrm{Ni}}$ ( $M_\odot$) | $M_{\mathrm{tr}}$ ( $M_\odot$) | $\rho_{\mathrm{tr}}$ ( $10^7$ g cm$^{-3}$ ) |
|---|---|---|---|---|---|
| deflagration models | | | | | |
| W7 | 1.38 | 1.3 | 0.60 | - | - |
| W70 | 1.38 | 1.3 | 0.60 | - | - |
| late detonation models | | | | | |
| W7DN | 1.38 | 1.4 | 0.60 | 1.20 | |
| W7DT | 1.38 | 1.5 | 0.78 | 1.08 | |
| W7DHE | 1.38 | 1.7 | 0.73 | 1.20 | |
| delayed detonation models | | | | | |
| WDD1 | 1.38 | 1.5 | 0.45 | | 3.0 |
| WDD2 | 1.38 | 1.5 | 0.58 | | 2.2 |
| WDD3 | 1.38 | 1.5 | 0.73 | | 1.7 |

and WDD1, respectively, where 3, 2, 1 indicate $\rho_7$ at the transition)(Nomoto et al. 1996). Figures 2.6-2.8 show the density, velocity, and composition structures of ejecta for the models WDD1-WDD3.

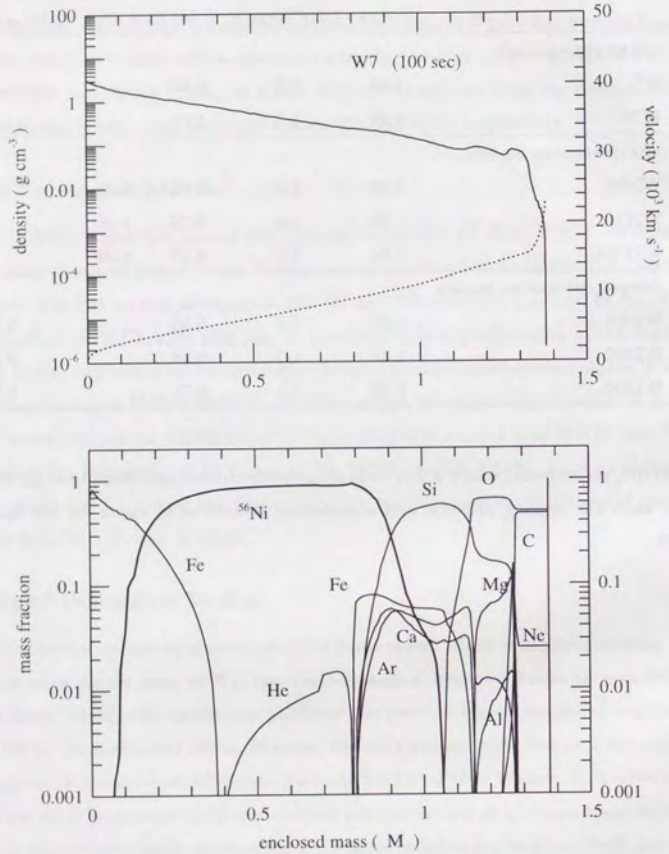


Figure 2.1: In the upper panel, the structure of the ejecta of W7 model model are shown: density(solid) and velocity(dotted) as a function of enclosed mass $M_r$ ( $M_\odot$ ). In the lower panel shown is the abundance distribution after the explosive nucleosynthesis.



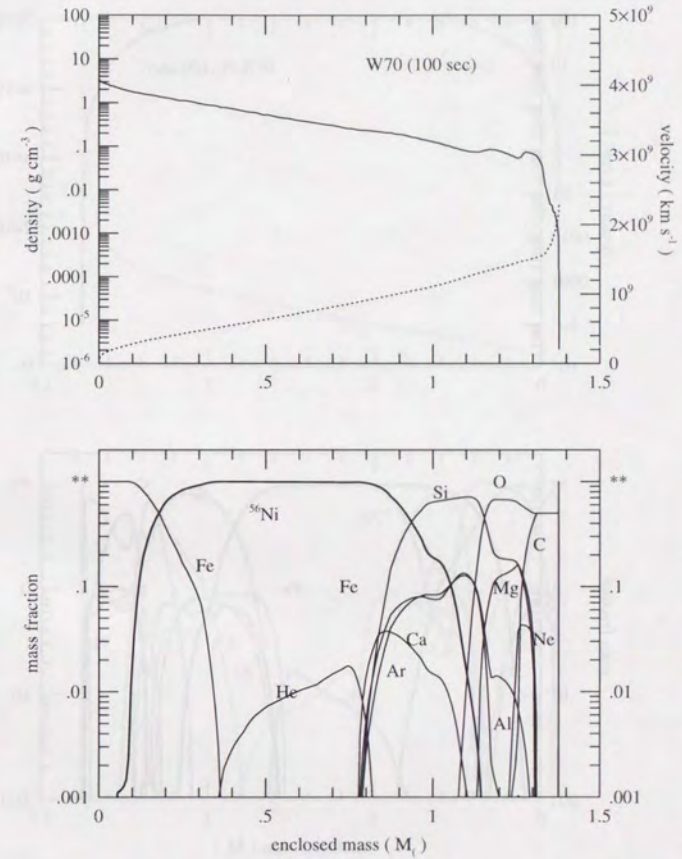


Figure 2.2: The Same figure as Figure 2.1 but for model W70.

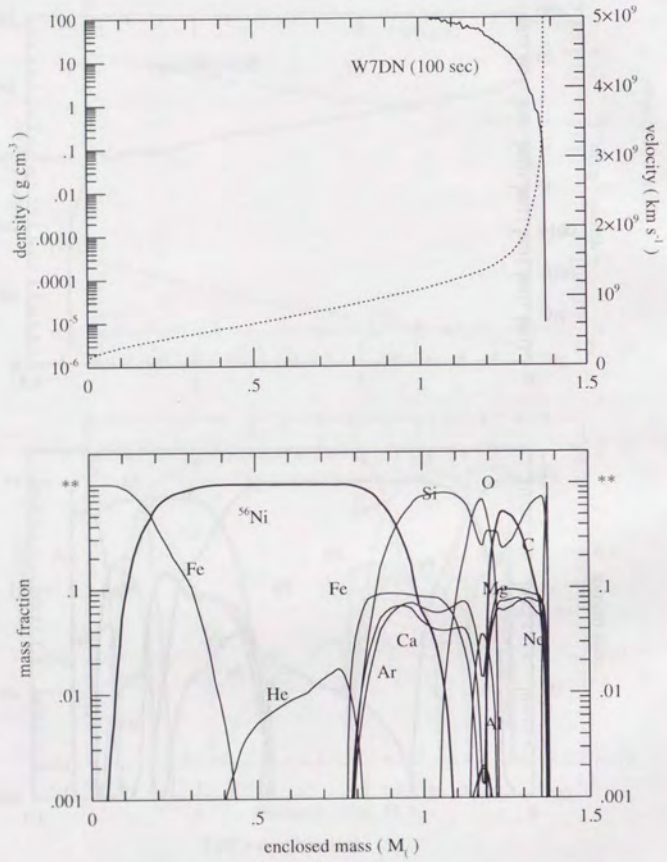


Figure 2.3: The Same figure as Figure 2.1 but for model W7DN.



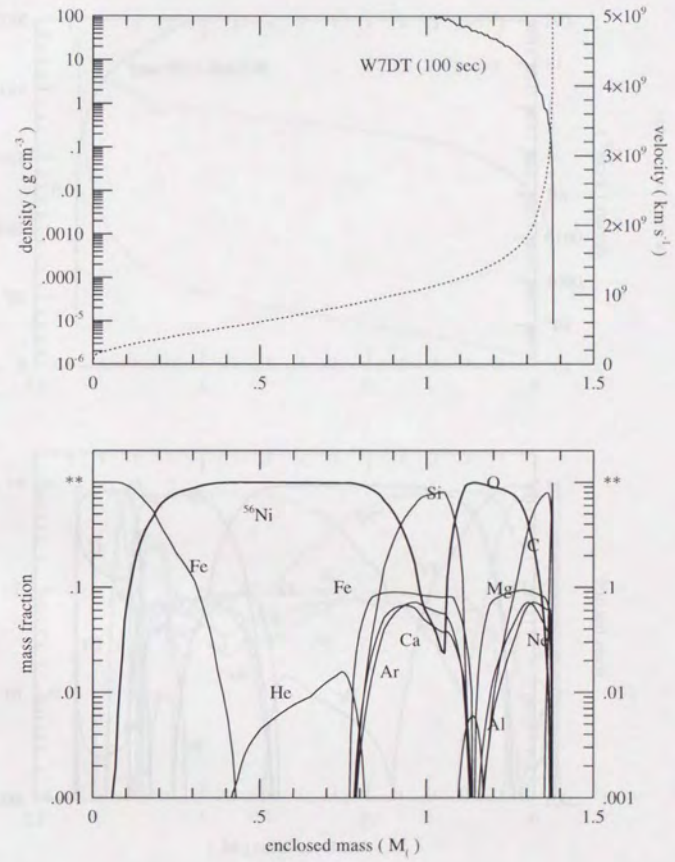


Figure 2.4: The Same figure as Figure 2.1 but for model W7DT.

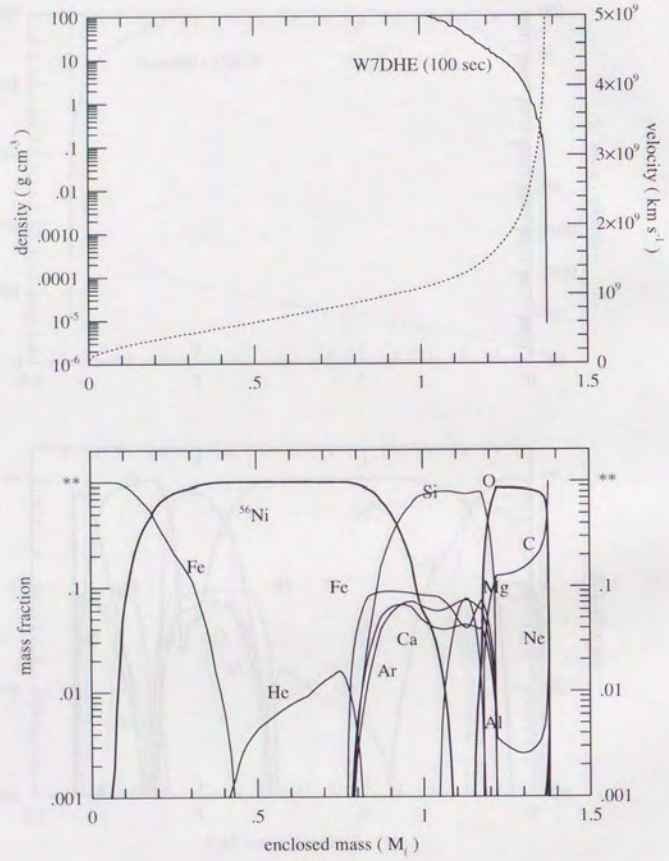


Figure 2.5: The Same figure as Figure 2.1 but for model W7DHE.



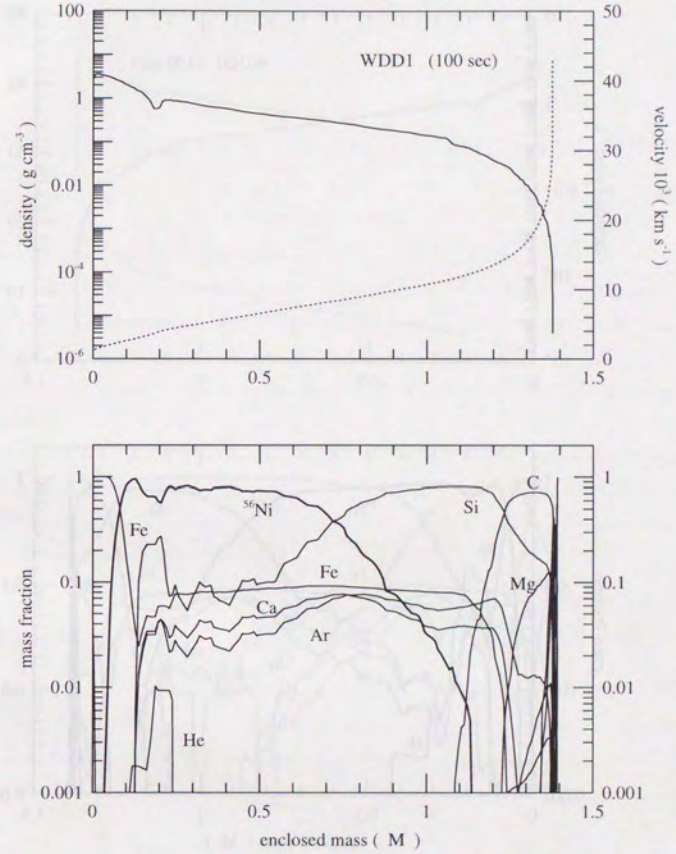


Figure 2.6: The Same figure as Figure 2.1 but for model WDD1.

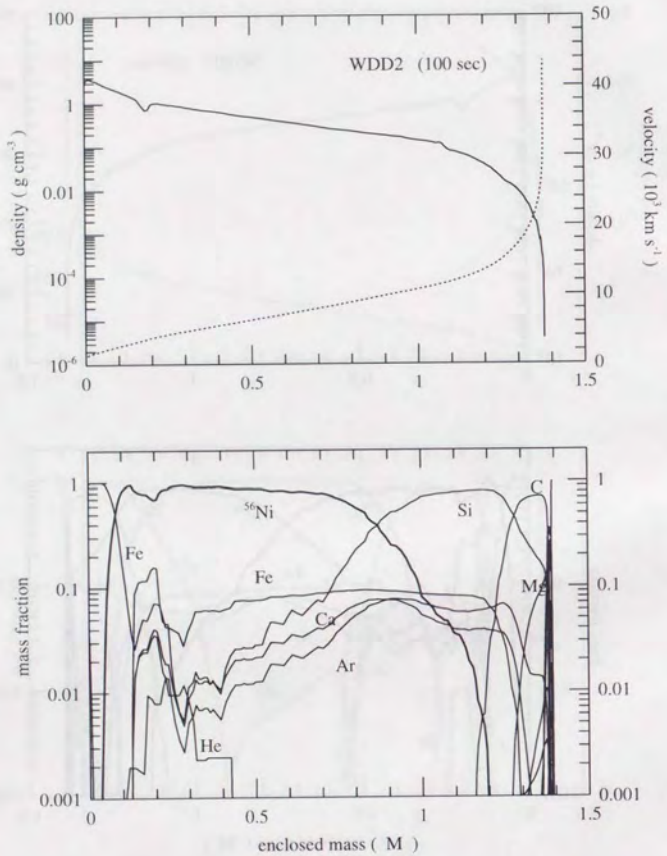


Figure 2.7: The Same figure as Figure 2.1 but for model WDD2.



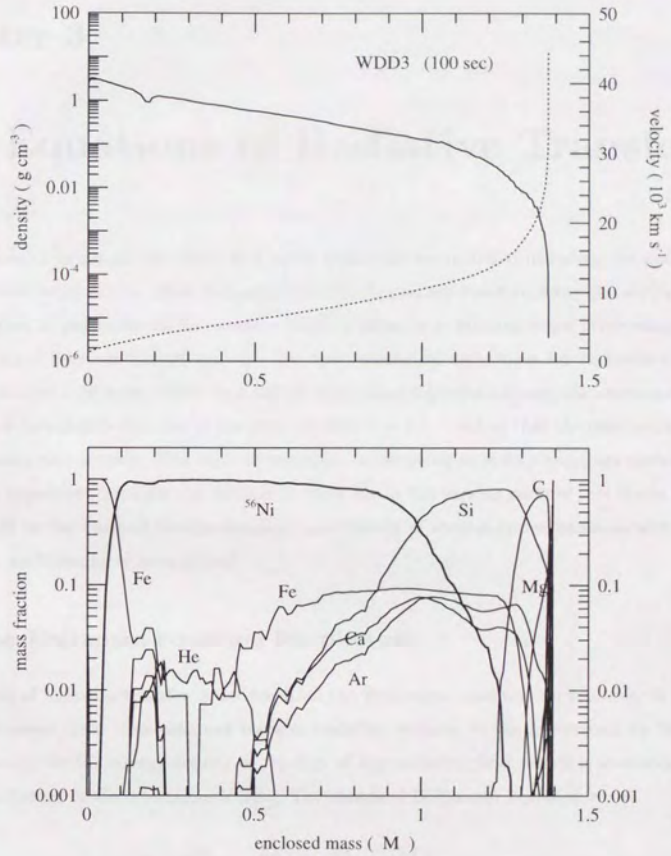


Figure 2.8: The Same figure as Figure 2.1 but for model WDD3.

# Chapter 3

# The Equations of Radiative Transfer

The fundamental issues on the radiative transfer equations are reviewed including the derivation and its physical implications. Most of the stuffs in this chapter are based on many pioneering works on this subject, in particular on an excellent book by Mihalas & Mihalas which gives comprehensive descriptions both on the physics and the basic numerical techniques for radiative transfer problems(Mihalas & Mihalas 1984). In a rapidly expanding supernova ejecta, the outermost layer is accelerated to a sizable fraction of the speed of light $\beta = v/c \sim 0.1$ so that the relativistic effect has to be taken into account. The transfer equations accurate up to order $O(v/c)$ are derived and some of the important formulae are defined for later use in the various parts of this thesis. These materials will be the basis of the discussion on the validity of various approximations with which the transfer problems have been solved.

## 3.1 The Boltzman equation for photons

The equation of radiative transfer is derived from the Boltzmann equation for photons. It should be noted, however, that thus obtained transfer equation reduces, in the free-streaming limit, to a wave equation for the energy density or the flux of the radiation field, which is consistent with the classical theory of electro-magnetic field. The standard Boltzmann equation reads

$$\frac{\partial f}{\partial t} + v_i \frac{\partial f}{\partial x_i} + \dot{p}_i \frac{\partial f}{\partial p_i} = \left(\frac{\delta f}{\delta t}\right), \tag{3.1}$$

where $v_i = \dot{r}_i$ and $(\delta f/\delta t)$ is the collision term. The distribution function $f = f(x, p, t)$ defines the occupation number of particles in the sense that the number of the particles in a volume $d^3r d^3p$ is equal to $dN = f d^3r d^3p$. The rigorous derivation of the relativistic Boltzman equation for photons has been given by Lindvigt(1966) with the definition of $f$ by Synge(1957). Without following the complete derivation, it is easy to see that equation (3.1) is generalized to a covariant form:

$$\frac{dx^\alpha}{d\tau}\frac{\partial f}{\partial x^\alpha} + \frac{dp^\alpha}{d\tau}\frac{\partial f}{\partial p^\alpha} = \left(\frac{\delta f}{\delta \tau}\right). \tag{3.2}$$

where $\tau$ is the proper time and $p^\alpha$ is the four-momentum of the photon. As the photon travels on the null cone surface, the affine length $\lambda$ defined as $p^\alpha \equiv dx^\alpha/d\lambda$, instead of $\tau$, is taken as a parameter for indicating the photon paths. Replacing the collision term with the source and extinction terms representing the emission and absorption of the photon by the material, the Boltzmann equation for photons can be written as

$$p^\alpha \frac{\partial f}{\partial x^\alpha} + \dot{p^\alpha}\frac{\partial f}{\partial p^\alpha} = \epsilon - \alpha f, \tag{3.3}$$

where $\dot{p^\alpha} = dp^\alpha/d\lambda$. Using the fact that the geodesics of the photon is expressed as

$$\frac{dp^\alpha}{d\lambda} + \Gamma^\alpha_{\beta\gamma} p^\beta p^\gamma = 0, \tag{3.4}$$

where $\Gamma^\alpha_{\beta\gamma}$ is the Christoffel symbols that are given by spacetime metric, we obtain the Boltzmann equation for photons in the general spacetime:

$$p^\alpha \mathcal{D} f = \epsilon - \alpha f, \tag{3.5}$$

where $\mathcal{D}$ is the operator defined as

$$\mathcal{D} = \frac{\partial}{\partial x^\alpha} - \Gamma^\beta_{\alpha\gamma} p^\gamma \frac{\partial}{\partial p^\beta} \tag{3.6}$$

In inertial frames, the photon trajectory is a straight line and the photon four-momentum is conserved $dp^\alpha/d\lambda = 0$ because all the components of the Christoffel symbols vanishes reflecting the flat spacetime in the absence of the general relativistic effects.

Using the explicit form of the photon four-momentum in Cartesian coordinates in the inertial frame,

$$p^\alpha = \frac{h\nu}{c}(1, \mathbf{n}), \tag{3.7}$$

we can write the transfer equation in terms of the specific intensity $I = (2h\nu^3/c^2)f$ as

$$\frac{1}{c}\frac{\partial I(\mathbf{n},\nu)}{\partial t} + \mathbf{n}\cdot\nabla I(\mathbf{n},\nu) = \eta - \chi I(\mathbf{n},\nu). \tag{3.8}$$

Here $\eta$ and $\chi$ is the emissivity and the extinction which appears in the radiative transfer equation the of familiar form. From the definition of the specific intensity $I$, it is clear that the quantity $I/\nu^3$ is a Lorenz invariant that is referred to as *invariant intensity*. Comparing the righthand side of equations (3.3) and (3.8), it is easy to see that $\eta/\nu^2$ and $\chi\nu$ are also the Lorenz invariants.



## 3.2 The Transfer Equation in the Comoving Frame

There are two kinds of frame in which the transfer equation is usually solved. One is the *inertial frame* and the other is the *comoving frame* which attaches to a fluid parcel at each point. Obviously the *comoving frame* is identical with the *Lagrangian frame* in fluid dynamics, or with the *proper frame* in relativistic term. In the comoving frame we can handle the microscopic interaction between radiation and matter in the most simple way at the cost of some complexity in the equations arising from the additional terms with frequency derivative and velocity-dependence. In this thesis, all the transfer equations are dealt with in the comoving frame as most of the other works in this field do so.

The comoving-frame transfer equation can be derived by starting with the inertial-frame equation and transforming all the relevant terms following the law of special relativity. Then we obtain the equation correct to all orders in $v/c$. Alternately, we can also start from the very beginning with the equation in a non-inertial frame if we only aim at obtaining the results with accuracy up to order $O(v/c)$. In the latter case, it can simply be done by applying the covariant form of the equation described in the previous section (3.5). For one-dimensional spherically symmetric flow, with the explicit form of the metric,

$$ds^2 = -c^2dt^2 + dr^2 + r^2(d\theta^2 + \sin\theta^2 d\phi^2), \tag{3.9}$$

we can evaluate the Christoffel symbols appearing in the operator (3.6). After some tedious but straightforward algebra, the radiative transfer equation in the comoving frame, in terms of the specific intensity $I_\nu = I(r,\mu,\nu,t)$, can be obtained as

$$\begin{aligned}
\frac{1}{c}\frac{DI_\nu}{Dt} &+ \frac{\mu}{r^2}\frac{\partial}{\partial r}(r^2 I_\nu) \\
&+ \frac{\partial}{\partial \mu}\left\{(1-\mu^2)\left[\frac{1}{r} + \frac{\mu}{c}\left(\frac{v}{r} - \frac{\partial v}{\partial r}\right) - \frac{a}{c^2}\right] I_\nu\right\} \\
&- \frac{\partial}{\partial \nu}\left\{\nu\left[(1-\mu^2)\frac{v}{cr} + \frac{\mu^2}{c}\frac{\partial v}{\partial r} + \frac{\mu a}{c^2}\right] I_\nu\right\} \\
&+ \left[(3-\mu^2)\frac{v}{cr} + \frac{1+\mu^2}{c}\frac{\partial v}{\partial r} + \frac{2\mu a}{c^2}\right] I_\nu \\
&= j_\nu - \kappa_\nu I_\nu - \sigma_\nu I_\nu + \frac{1}{4\pi}\int \sigma_\nu I_\nu d\Omega
\end{aligned} \tag{3.10}$$

where $\mu$ is the cosine of the angle between the outward radial direction and that of the photon propagation, $j_\nu$ is the emissivity, and $\kappa_\nu, \sigma_\nu$ are the absorption and scattering coefficients, respectively. $D/Dt$ is the Lagrangian derivative that is defined as $D/Dt = \partial/\partial t + \mathbf{v}\cdot\nabla$. It is tacitly assumed here that the scattering is elastic and isotropic, which is nearly valid in electron scatter-

ing but not true in line scattering in the present case of SNe Ia ejecta, which we will discuss later. In homologously expanding supernova ejecta, the matter acceleration is equal to zero ( $a = 0$ ) at every place so that the velocity remains constant $v = v(M_r)$ and the radius grows obeying $r = vt$ as time goes on. Note, however, it is not realized at early phase of the explosion. Our code is designed to be applicable to such cases which we really encounter in an extended SNe II envelope right after the shock breakout. If we restrict ourselves to consider the thermal emission process, in other words, we assume the local thermodynamic equilibrium(LTE), the emissivity can be written with the Planck function $B_\nu(T)$ as $j_\nu = \kappa_\nu B_\nu(T)$, where $T$ is the local gas temperature in statistical equilibrium. With these assumptions, the righthand side can be cast into a simple form,

$$\chi_\nu(S_\nu - I_\nu). \tag{3.11}$$

Here $\chi_\nu$ is the total extinction coefficient $\chi_\nu = \kappa_\nu + \sigma_\nu$ and $S_\nu$ is the source function that is defined as

$$S_\nu = \frac{\kappa_\nu B_\nu + \sigma_\nu J_\nu}{\kappa_\nu + \sigma_\nu}, \tag{3.12}$$

where $J_\nu$ is the mean intensity of the radiation field:

$$J_\nu = \frac{1}{4\pi}\int I_\nu d\Omega = \frac{1}{2}\int_{-1}^{1} I_\nu \mu d\mu. \tag{3.13}$$

In the actual light curve calculation in the present work, we solve the time-dependent transfer equation with multi-angle and multi-frequency groups in the exact form presented above. All the terms are properly included in the difference equations. The frequency derivative terms are important to take into account the Doppler effects due to the relative motion in the ejecta. In homologously expanding supernova ejecta, the observer at any point sees that the surrounding matter moves away from himself so that he always observes the incident photons redshifted as in the expanding universe. This effect is important in evaluating flux weighted and energy weighted opacities which appears in the frequency-integrated moment equations. In addition, it is inevitable to adopt multi-angle groups in order to calculate the Eddington factors which are required in solving the moment equations. We keep the time derivative in the equation, which has often been neglected in the previous works for computational simplicity. We found that it could make big differences especially at the dynamical diffusion phase and even at the nearly free-streaming phase in our comoving formulation.



## 3.3 Moments of the Transfer Equation

The first three moments of the specific intensity with respect to the angle give the monochromatic radiation energy density, flux, and pressure:

$$E_\nu = \frac{2\pi}{c}\int_{-1}^{1} I_\nu d\mu, \tag{3.14}$$

$$F_\nu = 2\pi\int_{-1}^{1} I_\nu \mu d\mu, \tag{3.15}$$

$$P_\nu = \frac{2\pi}{c}\int_{-1}^{1} I_\nu \mu^2 d\mu. \tag{3.16}$$

It is worthwhile deriving here the transformation formula of the monochromatic flux from the comoving to the inertial frame, which is needed to calculate the observer's frame flux or luminosity from the comoving frame solutions. The Lorentz transformation for $\nu$ and $\mu$ accurate to the first order in $v/c$ goes like

$$\nu = \nu_0(1 + \beta\mu_0), \tag{3.17}$$

$$\mu = \frac{\mu_0 + \beta}{1 + \beta\mu_0}, \tag{3.18}$$

where the variables with and without the subscript 0 designate the comoving-frame and the inertial-frame quantities, respectively. Using equations (3.17) and (3.18), the transformation law of $I_\nu$, we have

$$\begin{aligned}
F_\nu &= 2\pi\int_{-1}^{1} I(\mu,\nu)\mu d\mu \\
&= 2\pi\int_{-1}^{1}\left(\frac{\nu}{\nu_0}\right)^3 I^0(\mu_0,\nu_0)d\mu \\
&= 2\pi\int_{-1}^{1}(1+\beta\mu_0)\left\{I^0(\mu_0,\nu) + (\nu_0-\nu)\frac{\partial I^0}{\partial\nu}\right\}d\mu_0 \\
&= 2\pi\int_{-1}^{1}\left\{\mu_0 + \beta(1+\mu_0^2)\right\}I^0 d\mu_0 - 2\pi\int_{-1}^{1}\beta\frac{\partial}{\partial\nu}(\nu\mu_0^2 I^0)d\mu_0 \\
&= F_\nu^0 + v(E_\nu^0 + P_\nu^0) - \nu\frac{\partial}{\partial\nu}(\nu P_\nu^0).
\end{aligned} \tag{3.19}$$

Similarly, for the monochromatic radiation energy density, we have

$$E_\nu = E_\nu^0 + \frac{2v}{c^2}F_\nu^0 - \frac{v}{c^2}\frac{\partial}{\partial\nu}(\nu F_\nu^0). \tag{3.20}$$

Integrating equation (3.10) against $d\mu$ and $\mu d\mu$ in the comoving frame, we obtain the monochromatic radiation energy and momentum equations, respectively. Carrying out further integration over comoving frequency, we eventually have the following radiation energy and momentum equations,

$$\frac{DE}{Dt} = -\nabla \cdot \mathbf{F} - \frac{v}{r}(3E - P) - \frac{\partial v}{\partial r} + \int_0^\infty (4\pi\eta - c\chi E) d\nu, \tag{3.21}$$

$$\frac{1}{c^2}\frac{DF}{Dt} = -\nabla \cdot \mathbf{P} - \frac{2}{c^2}\left(\frac{\partial v}{\partial r} - \frac{v}{r}\right) F - \frac{1}{c}\int_0^\infty \chi F d\nu. \tag{3.22}$$

where $E$ and $F$ are the radiation energy density and the radiative flux, respectively, which are defined as

$$E = \int_0^\infty E_\nu d\nu, \tag{3.23}$$

$$F = \int_0^\infty F_\nu d\nu, \tag{3.24}$$

and $\mathbf{F}$ and $\mathbf{P}$ denote the flux vector and the radiation pressure tensor, respectively. In general, the radiation pressure is not a scalar but a tensor, whose components have the following expressions in spherical symmetry,

$$P_{ij} = \begin{pmatrix} P & 0 & 0 \\ 0 & \frac{1}{2}(E-P)/r^2 & 0 \\ 0 & 0 & \frac{1}{2}(E-P)/r^2 \sin^2\theta \end{pmatrix}, \tag{3.25}$$

where subscripts $i = 1, 2, 3$ denote $(r, \theta, \phi)$, respectively. The divergences of the pressure tensor and the flux vector are written as

$$\nabla \cdot \mathbf{P} = \frac{\partial P}{\partial r} + \frac{3P - E}{r}, \tag{3.26}$$

$$\nabla \cdot \mathbf{F} = \frac{1}{r^2}\frac{\partial}{\partial r}(r^2 F). \tag{3.27}$$

The ratio of two scalars $P$ and $E$ defines the scalar Eddington factor $f$:

$$f = \frac{P}{E}. \tag{3.28}$$

Let us consider a radiation field with constant intensities over solid angles $2\pi(1 - \mu_0)$ from $\mu = \mu_0$ to 1. In this case we obtain the Eddington factor,



$$\begin{aligned} f &= \frac{\int_{\mu_0}^1 I\mu^2 d\mu}{\int_{\mu_0}^1 I d\mu} \\ &= \frac{1}{3}(\mu_0^2 + \mu_0 + 1) \\ &= \frac{1}{3}\left(\mu_0 + \frac{1}{2}\right)^2 + \frac{1}{4}. \end{aligned} \tag{3.29}$$

An isotropic radiation has an exact value of $f = 1/3$ as easily seen if we put $\mu_0 = -1$ in (3.27). The maximum value of $f = 1$ will be attained when one preferred direction exists in the radiation field. It is easy to see that $f \to 1$ if we take the limit of $\mu_0 \to 1$. Normally, $f$ lies between 1/3 and 1. But, in some cases it could be smaller than 1/3. We can see that in the above simplified model $f$ has a minimum of 1/4 when $\mu_0 = -1/2$. It could be possible, for instance, at some depth points just beneath the photosphere.

## 3.4 Radiation Hydrodynamics

As well as solving the transfer equation, we have also to determine the structure and evolution of the gas temperature consistently with the radiation field. To do this, we need to solve a coupled system of equations of the hydrodynamics of gas content and the radiative transfer. This sort of problem is commonly called the *radiation hydrodynamics*. The gas momentum equation is expressed as

$$\rho\frac{\partial v}{\partial t} = -\frac{GM_r\rho}{r^2} - \frac{\partial P}{\partial r} + \frac{1}{c}\int_0^\infty \chi F_\nu, \tag{3.30}$$

which means that the change of the gas momentum is caused by the self-gravitational force, the pressure gradient force and also by the radiative acceleration force. The gas energy equation is written as

$$\rho\left[\frac{De}{Dt} + P\frac{D}{Dt}\left(\frac{1}{\rho}\right)\right] = \int_0^\infty (c\chi E - 4\pi\eta) d\nu + \rho\epsilon \tag{3.31}$$

where the second term in the lefthand side comes from the $PdV$ work and the first two terms in the righthand side from the interaction between matter and radiation, the absorption and the emission, respectively. The last term in the righthand side represents the energy deposition due to the gamma-rays from radioactive decays of $^{56}$Ni and $^{56}$Co.

We use the mass coordinate $M_r$ that is defined by $dM_r = 4\pi r^2 \rho dr$ instead of the radius $r$. The complete set of the equations that are actually solved in our work are summarized as follows. The time derivatives are all in the Lagrangian sense.

$$\frac{\partial v}{\partial t} = -\frac{GM_r}{r^2} - 4\pi r^2 \frac{\partial P}{\partial M_r} + \frac{\chi_F F}{\rho c} \tag{3.32}$$

$$\frac{\partial r}{\partial t} = v \tag{3.33}$$

$$\frac{\partial}{\partial M_r}\left(\frac{4\pi}{3}r^3\right) = \frac{1}{\rho} \tag{3.34}$$

$$\frac{\partial}{\partial t}\left(e + \frac{E}{\rho}\right) = \epsilon - (P + fE)\frac{\partial}{\partial t}\left(\frac{1}{\rho}\right) - 4\pi\frac{\partial}{\partial M_r}(r^2 F) + (3f-1)\frac{vE}{\rho r} \tag{3.35}$$

$$\frac{\partial}{\partial t}\left(\frac{E}{\rho}\right) = \frac{c}{\rho}(\kappa_P a T^4 - \kappa_E E) - fE\frac{\partial}{\partial t}\left(\frac{1}{\rho}\right) - 4\pi\frac{\partial}{\partial M_r}(r^2 F) + (3f-1)\frac{vE}{\rho r} \tag{3.36}$$

$$\frac{\partial F}{\partial t} = -\left(c\chi_F + \frac{2v}{r}\right)F - 4\pi r^2 \rho\left(c^2\frac{\partial(fE)}{\partial M_r} + 2F\frac{\partial v}{\partial M_r}\right) - (3f-1)\frac{c^2 E}{r} \tag{3.37}$$

The gas energy equation is replaced by the total energy equation for gas and radiation field (3.35), which is obtained by adding the equations (3.21) and (3.31). In equation (3.36) $a$ denotes the radiation energy density constant defined by

$$a = \frac{8\pi^5}{15}\frac{k_B^4}{h^3 c^3} = 7.56 \cdot 10^{-15}\mathrm{ergcm^{-3}K^{-1}}. \tag{3.38}$$

The mean opacities that appears in the above equations are the Planck mean and energy mean opacities ($\kappa_P$, $\kappa_E$) for absorption part and the flux mean opacity ($\chi_F$) for total extinction ($\chi = \kappa + \sigma$):

$$\kappa_P = \frac{\int B_\nu(T)\kappa_\nu d\nu}{\int B_\nu(T) d\nu}, \tag{3.39}$$

$$\kappa_E = \frac{\int E_\nu \kappa_\nu d\nu}{\int E_\nu d\nu}. \tag{3.40}$$

$$\chi_F = \frac{\int F_\nu \chi_\nu d\nu}{\int F_\nu d\nu}. \tag{3.41}$$

The flux mean opacity reduces to the Rosseland mean opacity ($\chi_{Ross}$) if the radiation field is nearly isotropic and in the so called diffusion regime. Replacing the $F_\nu$ in (3.40) by $-\frac{1}{\chi_\nu}\frac{\partial B_\nu}{\partial T}$ which is the flux in the diffusion limit, we obtain

$$\chi_{Ross} = \frac{\int \frac{\partial B_\nu}{\partial T} d\nu}{\int \frac{1}{\chi_\nu}\frac{\partial B_\nu}{\partial T} d\nu}. \tag{3.42}$$



The Planck mean and the Rosseland mean opacity can be calculated if the local gas temperature and the chemical abundances are given. But, to evaluate the energy mean and the flux mean opacities, we need the monochromatic energy density and flux of the radiation field. Assuming the LTE, we can tabulate the monochromatic opacity as a function of the density, temperature, and the chemical compositions for each zone. Using this table, we perform the frequency integrations in (3.38)-(3.40) to calculate the mean opacities at each time step.

# Chapter 4

# Preliminary Inquiries with Grey Opacities

A radiation transfer problem in which the opacity is assumed to be constant independently of frequency is called grey problem. The grey problem allows us to look into some general aspects of radiative transfer which do not depend on specific characteristics of the material considered. In this chapter, to see qualitative behavior of the light curve of SNe Ia, we present some analytic arguments with grey opacities under the diffusion approximation. Then, we calculate the light curve of W7 model with grey opacities to test our numerical code and to see the light curve sensitivities on the opacity and the nickel mass.

## 4.1 Light Curve Analysis with Simple Models

A light curve modeling with analytic solutions was first presented by Arnett(1982). He assumed a constant density sphere that expands homologously and derived an ordinary differential equation that describes its thermal evolution with the diffusion approximation. The system of transfer equation and gas energy equation reduces to an eigenvalue problem there. The basic light curve properties are well reproduced though qualitatively by such a simple model. Recently, Pinto & Eastman(1996) extended the analysis by Arnett to take into account the non-uniform ejecta structure including higher order modes of the eigenfunctions. Instead of reviewing these works, we present more basic arguments on the general characteristics of the light curve shape.

In general, light curves are characterized by the quantities such as peak magnitude, rising time to maximum, and declinig rate in tail. These quantities depend on the hydrodynamical models, the total mass of the ejecta($M_{\rm ej}$), or the explosion energy($E$). The rising time or the peak width of the light curve can be roughly estimated by equating the diffusion time scale $\tau_{\rm diff} \sim \kappa\rho R^2$ with

the dynamical time scale $\tau_{\rm dyn} \sim R/v_{\rm exp}$,

$$\tau_{\rm diff} \sim \tau_{\rm dyn}. \tag{4.1}$$

In a homologously expanding sphere, the radius is given by $R \sim v_{\rm exp}t$ with the expansion velocity $v_{\rm exp}$. Using the fact that the density decreases as $\rho \sim M_{\rm ej}/R^3 \propto t^{-3}$, we obtain the characteristic time scale of the light curve ($\tau_{\rm LC}$) as

$$\tau_{\rm LC} \sim \left(\frac{\kappa M_{\rm ej}}{v_{\rm exp}}\right)^{1/2}. \tag{4.2}$$

The explosion energy approximately scales as

$$E \sim \frac{1}{2}M_{\rm ej}v_{\rm ej}^2 \sim \epsilon M_{\rm Ni}, \tag{4.3}$$

where $M_{\rm Ni}$ is the nickel mass and $\epsilon$ the nuclear energy release per unit mass when C+O mixture is burned into nickel. Solving equation (4.3) for $v_{\rm ej}$ and substituting it into equation (4.2), we eventually have the relation

$$\tau_{\rm LC} \propto \frac{\kappa^{1/2}M_{\rm ej}^{3/4}}{M_{\rm Ni}^{1/2}}. \tag{4.4}$$

For the Chandrasekhar mass explosions, $M_{\rm ej}$ is nearly the same for all models, while $M_{\rm Ni}$ could be different depending on the flame speed of the burning front. The larger nickel mass corresponds to the higher expansion velocity and the faster evolving light curve due to larger amount of nuclear energy release. This comes to a prediction that *brighter* SNe Ia decline *faster*. On the other hand, for sub-Chandrasekhar mass models, $M_{\rm Ni}$ varies approximately in proportional to $M_{\rm ej}$. Therefore, the larger mass explosion is expected to produce the *brighter* and *slower* light curves, which was the observed trend suggested by Phillips(1993).

However, we should also take the opacity effect into consideration. Before or near the maximum light, the opacity is dominated by two comparable sources, the electron scattering and the line opacity. The electron scattering opacity is larger at higher temperature, while the line opacity shows several peaks at moderate temperatures. In addition, the line opacity could change in a complicated mannar, firstly due to their enhancement at earlier phase by expansion effect and secondly due to its dependence on the chemical composition.

In general, the larger nickel mass means the higher temperature of ejecta, thus resulting in larger $\kappa$, provided that the electron scattering is the only opacity source. This effect might explain the *brighter-slower* relation of the light curve. But, the larger $\kappa$ favors the longer rise time, unless the nickel mass is remarkably large.



## 4.2 Test Problem with Grey Opacities

Here we present both bolometric and monochromatic light curves for model W7 with grey opacities. As is discussed in the preceding section, the light curve variations according to the different nickel masses and opacities are not so simple within quantitative precisions. For the Chandrasekhar mass models, the nickel mass and thus the expansion velocity must be similar to those of the model W7 to be consistent with the line features in the observed spectra of SNe Ia. Thus, we calculate three cases artificially changing the nickel mass. The nickel is assumed to be concentrated in the central spherical core.

Figure 4.1 shows $U, B, V$ and bolometric light curves with $M_{\rm Ni} = 0.4, 0.6$, and $0.8\ M_\odot$ assuming constant opacity $\kappa = 0.1$. As is expected, the larger mass model has the brighter magnitude and wider peak width in the bolometric light curve. Because of the grey opacity, most of the photons seem to be emitted in the $U$ band near maximum light. Therefore, $U$ is similar to the bolometric but $B$ and $V$ are different and do not show expected nickel mass dependence of the peak magnitude. In the tail phase, the nickel mass determines the absolute magnitude but does not affect the declinig rate.

Figure 4.2 shows the same light curves for W7 with the same nickel mass $M_{\rm Ni} = 0.6$ but for different values of constant opacity $\kappa = 0.1, 0.2$ and $0.3$. We find that smaller opacity produces earlier rise and faster decline of the light curve. One interesting point is that monochromatic light curves in each color band show some variations in the declining rate during several ten days after maximum whereas the bolometric does not show such tendencies. Since the grey opacity is a clude approximation in the case of real SNe Ia, it is not meaningful to discuss these results in detail. These stuffs tell no more than just confirm the expected light curve trend we discussed earlier.

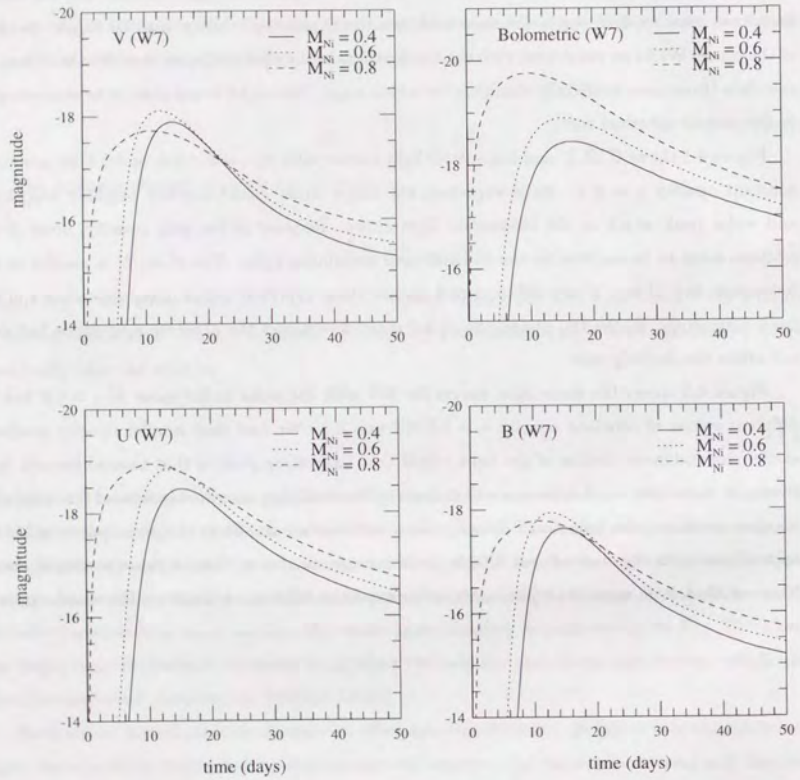


Figure 4.1: Monochromatic light curves with different nickel mass. Three different cases for $M_{\rm Ni} = 0.4$ (solid), $M_{\rm Ni} = 0.6$ (dotted), and $M_{\rm Ni} = 0.8$ (dashed) are calculated for W7 with $\epsilon = 0.1$.



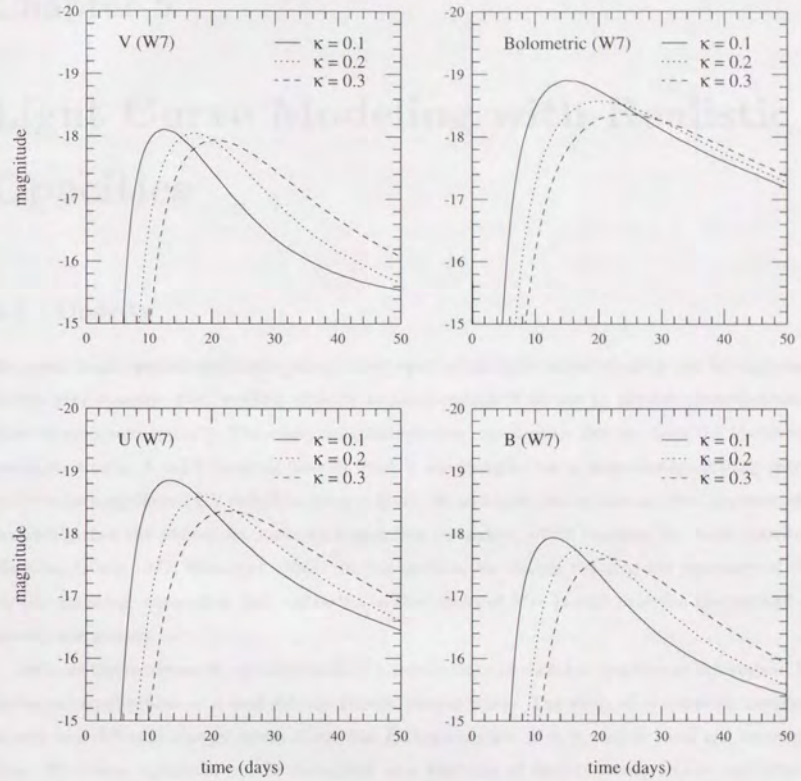


Figure 4.2: Monochromatic light curves with different opacities. Three different cases for $\kappa = 0.1$ (solid), $\kappa = 0.2$ (dotted), and $\kappa = 0.3$ (dashed) are calculated for W7 with $\epsilon = 0.1$.

# Chapter 5

# Light Curve Modeling with Realistic Opacities

## 5.1 Opacity

As shown in the preceding chapter, the general trend of the light curve behavior can be explained by the grey opacity. But, realistic opacity is indispensable if we are to predict monochromatic light curves quantitatively. The emergent spectrum can significantly deviate from the blackbody one in its shape. A thick forest of lines in the UV wavelengths has a large line-blanketing effect, which causes significant UV deficit in the spectrum. In addition, the expansion effect increases the possibility that the photon interacts with each line resonance, which increase the mean opacities effectively(Karp 1977; Blinnikov 1995). In this section, we discuss the physical processes of the photon emission, absorption and scattering in the ejecta of SNe Ia and describe the method of opacity calculation.

In local thermodynamic equilibrium(LTE), populations of each ion species are determined by statistical equilibrium at a well-defined kinetic temperature. The ratio of occupation numbers at any two different energy levels obeys the Boltzmann law with a unique local gas temperature. Therefore, opacities can be tabulated as a function of density, temperature, and chemical composition at each layer. To determine the ionization balance and the electron number density, we solve Saha-Boltzmann equations including all ionization stages of 13 elements (H,He,C,N,O,Ne,Na,Mg,Al,Si,Ar,Ca,Fe),

$$\frac{n_{ij+1}n_e}{n_{ij}} = \frac{2U_{ij+1}(T)}{U_{ij}(T)}\left(\frac{2\pi m_e k_B T}{h^2}\right)^{3/2} \cdot \exp\left(-\frac{\chi_{i,j}}{k_B T}\right). \tag{5.1}$$

Here $n_{ij}$ and $\chi_{ij}$ are the number density and the ionization potential of $j-$times ionized species of element $i$, respectively. $n_e$ is the electron number density. $U_{ij}$ is the partition function that is

defined as

$$U_{ij}(T) = \sum_k g_{ijk} \exp\left(-\frac{\epsilon_{ijk}}{k_B T}\right), \tag{5.2}$$

where $\epsilon_{ijk}$ and $g_{ijk}$ are the energy and the statistical weight of $k$-th level of $j-$times ionized species of element $i$. Atomic models, i.e., the ionization energy, the energy level and the statistical weight employed here are taken from the Opacity Project(Seaton 1993) except for FeI and FeII. For the two species , we use the database compiled by Kurucz(1993). From the solutions of Saha equations, we calculate the occupation number at each energy level as

$$n_{ijk} = \frac{N_{ij} g_{ijk}}{U_{ij}(T)} \exp\left(-\frac{\epsilon_{ijk}}{k_B T}\right). \tag{5.3}$$

With the electron number density and the occupation numbers at each atomic level, it is straightforward to calculate the monochromatic opacity. Since the number of energy groups for the actual transfer calculation is limited, we need some averaging procedure in frequency space. The total opacity in our calculations includes contributions from bound-bound, bound-free(photoionizaion), free-free(bremsstrahlung) transitions and Thomson scattering off free electrons. The absorptive and scattering parts of the opacity can be written as

$$\kappa_\nu = \epsilon(\chi_\nu^{\rm bb} + \chi_\nu^{\rm bf}) + \chi_\nu^{\rm ff}, \tag{5.4}$$

$$\sigma_\nu = (1-\epsilon)(\chi_\nu^{\rm bb} + \chi_\nu^{\rm bf}) + n_e \sigma_T. \tag{5.5}$$

with

$$\epsilon = \frac{\epsilon'}{1+\epsilon'}, \tag{5.6}$$

and

$$\epsilon' = (1 - e^{-h\nu/kT}) \frac{C_{ul}}{A_{ul}}, \tag{5.7}$$

where $\sigma_T$ is the Thomson scattering cross section and $\epsilon$ the fraction of the absorptive opacity. The ratio of the collisional deexcitation rate($C_{ul}$) and the Einstein spontaneous emission probability ($A_{ul}$) can be roughly estimated by Van Regemorter(1962) formula,

$$\frac{C_{ul}}{A_{ul}} = \frac{n_e}{T^{1/2}} \frac{10.339}{\nu/c^3}. \tag{5.8}$$

For bound-bound transitions, we average the line opacities over each frequency range with logarithmically equal interval as



$$\chi_\nu^{\rm bb} = \frac{1}{\Delta\nu} \sum_{\nu_j < [\nu_i, \nu_i + \Delta\nu]} \frac{h\nu}{4\pi} \phi(\nu_j) n_l B_{lu,j} (1 - e^{-h\nu/kT}), \tag{5.9}$$

where $1 - e^{-h\nu/kT}$ is the correction factor for stimulated emissions in LTE and $\phi(\nu)$ is the line profile function, which is normalized as

$$\int_0^\infty \phi(\nu) d\nu = 1. \tag{5.10}$$

The intrinsic line profiles are determined by the thermal Doppler broadening with a width of $\sim$ Å. Because of our coarse frequency grids of order $\sim 100$ Å, we assume the line profile to be a Dirac $\delta$-function. $B_{lu,j}$ is the Einstein $B$ coefficient for downward transition in $j$-th line, which is related to the $A$ coefficient $A_{lu}$ by

$$A_{lu} = \frac{2h\nu^3}{c^2} B_{lu}, \qquad g_l B_{lu} = g_u B_{ul}. \tag{5.11}$$

In terms of $gf$ values, Einstein $A$ coefficients are expressed as

$$A_{ul} = 6.70 \times 10^{15} \frac{gf}{g_u \lambda(\text{Å})^2} \text{sec}^{-1}. \tag{5.12}$$

The bound-free and free-free contributions are

$$\chi_\nu^{\rm bf} = \sum_i n_i \alpha_{ik}(\nu)(1 - e^{-h\nu/kT}), \tag{5.13}$$

$$\chi_\nu^{\rm ff} = \sum_i n_e n_i \alpha_\nu^{\rm ff} (1 - e^{-h\nu/kT}) \tag{5.14}$$

where the summation with regard to $i$ is taken for all species with bound electrons in *bound-free* and for all species except for neutral ones in free-free opacities. For photoionization cross sections $\alpha_{ik}(\nu)$, we use the fitting formulae given by Verner et al. (1996). The thermal bremsstrahlung(free-free) absorption coefficients are taken from Rybicki & Lightman(1979),

$$\alpha_\nu^{\rm ff} = 3.7 \times 10^8 Z_i^2 g_i^{\rm ff} \nu^{-3} T^{-1/2} \text{cm}^5. \tag{5.15}$$

where $Z_i$ is the charge of the ion and $g_i^{\rm ff}$ the gaunt factor of order unity. We take approximately $g_i^{\rm ff} = 1$ for all species, which does not affect the light curve modeling because the free-free contribution is negligibly small in the optical wavelengths at the relevant densities here.

Figure 5.1 and 5.2 show examples of the monochromatic opacity of pure iron plasma at $\rho = 10^{-13}$ g cm$^{-3}$ and $T = 2.5 \times 10^4$ K, a typical condition for the ejecta of SNe Ia near maximum light. A total of 1,000 or 100 wavelength grids with logarithmically equal intervals ( $\nu/\Delta\nu = 109$ *or* 10.9

) are used to average the line opacity in Figure 5.1 and 5.2, respectively. Actually, we take 100 frequency grids ranging from 1,000 Å to 20,000 Å for all LCv calculations in the present study.

## 5.2 Equation of State and Gamma Ray Deposition

The equation of state employed here is that of ideal gas composed of ions and electrons, which is a good approximation in the relevant conditions in the ejecta of SNe Ia,

$$P = (n_{ion} + n_e)k_B T. \tag{5.16}$$

The electron number density $n_e$ is given by the solutions of Saha equations and varies as the degree of ionization changes, while the number density of ion $n_{ion}$ is constant and has a value:

$$n_{ion} = \sum_i \frac{\rho X_i}{A_i m_u}, \tag{5.17}$$

where $X_i, A_i$ are the mass fraction, mass number of each element and $m_u$ the atomic mass unit.

The primary energy source to power the SNe Ia light curves are the radioactive decays of $^{56}$Ni and $^{56}$Co . The gamma ray deposition is important since it determines the heating rate and the thermal structure of the ejecta and therefore the absolute magnitude of SNe Ia. The most direct and reliable approach is the use of Monte Carlo simulations for absorption and scattering processes for high energy photons(Kumagai 1989). However, this method is too time consuming to obtain enough spatial resolutions to reflect the detailed distribution of the radioactive elements. In the present study, we adopt the most simplest method to save the computational time. We use a deposition function in the following form.

$$\dot{\epsilon}_{\gamma-ray} = X_{\rm Ni} f(r)\phi(t) \qquad \text{erg g}^{-1}\text{s}^{-1}, \tag{5.18}$$

with

$$f(r) = 0.04 + 0.96\left[1 - \exp\left(-\int_r^\infty \kappa_\gamma \rho dr\right)\right], \tag{5.19}$$

and

$$\phi(t) = 3.90 \times 10^{10} e^{-t/\tau_{\rm Ni}} + 6.29 \times 10^9 (e^{-t/\tau_{\rm Co}} - e^{-t/\tau_{\rm Ni}}), \tag{5.20}$$

where $\tau_{\rm Ni}$ and $\tau_{\rm Co}$ are the lifetime of $^{56}$Ni and $^{56}$Co , respectively, and $X_{\rm Ni}$ the initial mass fraction of $^{56}$Ni . We assume the effective absorption coefficient for $\gamma$-rays $\kappa_\gamma = 0.04$ that is obtained by Monte-Carlo simulations.



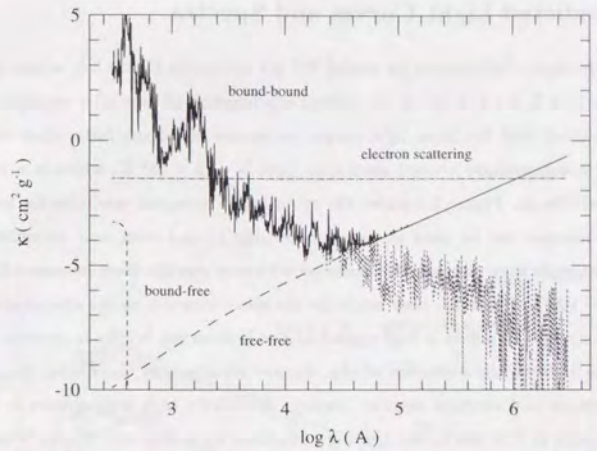


Figure 5.1: Monochromatic opacity of pure iron plasma at $\rho = 10^{-13}$ g cm$^{-3}$ and $T = 2.5 \times 10^4$ K with LTE assumption. A total of 1,000 wavelength grids are used ($\lambda/\Delta\lambda = 109$). The solid line shows the sum of all the contributions except for electron scattering. Other lines correspond to different sources as designated.

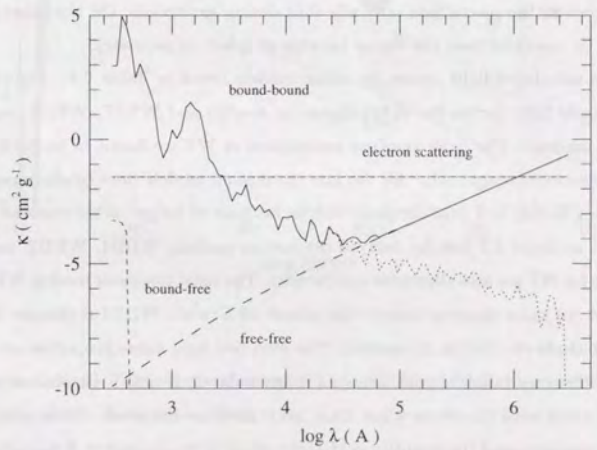


Figure 5.2: Monochromatic opacity at the same condition in Figure.5.1 but with 100 wavelength grids ($\lambda/\Delta\lambda = 10.9$).

## 5.3 Predicted Light Curves and Spectra

The monochromatic light curves for model W7 are plotted in Figure 5.3, where vertically shifted magnitudes, $U+2, B+1, V, R-1$ are plotted as a function of time after explosion. It reproduces the general trend that the bluer light curves rise earlier and decay faster than redder ones. The Photospheric temperature around maximum light is $\sim 2 \times 10^4$ K, which is a typical value for the observed SNe Ia. Figure 5.4 shows the evolution of emergent spectrum for model W7. Some absorption features can be seen at early phase (day 2) and even near maximum light(day 14, day 21), although they can not be identified with any specific lines because of poor frequency resolution $\sim 100$ Å. Probably, they might be the absortions due to the species such as SiII, FeII, or FeIII. A strong UV deficit is well reproduced as is observed in SNe Ia spectra.

Figure 5.5 shows the evolution of the thermal structure of the ejecta, the distributions of gas temperature and electron number density. Relatively high temperature is achieved in the layers abundant in $^{56}$Ni due to the heating by radioactive decays of $^{56}$Ni and $^{56}$Co . The electron number density steadily decreases reflecting the density drop and the changes in the degrees of ionizations according to the thermal balance between radioactive heating and cooling. The cooling is dominated by adiabatic expansion at earlier phases, gradually being replaced by radiative processes at later nebular phases. In Figure 5.6, the inertial frame luminosity and the Eddington factors are plotted against the enclosed mass. It is seen that the Eddington factor is increasing in outer layers as the ejecta gets optically thin during expansion. On the other hand, it always remains to be one third near the center because of spherical geometry.

We also calculated light curves for other models listed in Table 2.1. Figure 5.7 shows the monochromatic light curves for W7(deflagration model) and W7DT, W7DN, and W7DHE(late detonation models). The peak aboslute magnitudes of W7 are found to be -18.8 in $B$ band and - 19.0 in bolometric magnitude. All the late detonation models have brighter peak luminosities, shorter rising times, and broader peak widths because of larger nickel masses. Figure 5.8 is a similar plot as figure 5.7 but for delayed detonation models, WDD1, WDD2, and WDD3. The light curves for W7 are also shown for comparison. The most luminous models WDD2 and WDD3 have almost the same absolute magnitudes about -19.5, while WDD1 is dimmer than W7 having a peak magnitude of - 18.6 in bolometric. The obtained light curve properties are summarized in Table 5.1, where we tabulate peak absolute magnitudes in $B$ and $V$ bands and peak bolometric magnitude along with the times when these maximum are achieved. Other contents are $B-V$ color at $V$ maximum and the quantity $\Delta M_{15}(B)$, which is the amount of $B$ magnitude drop during first 15 days after its maximum light.



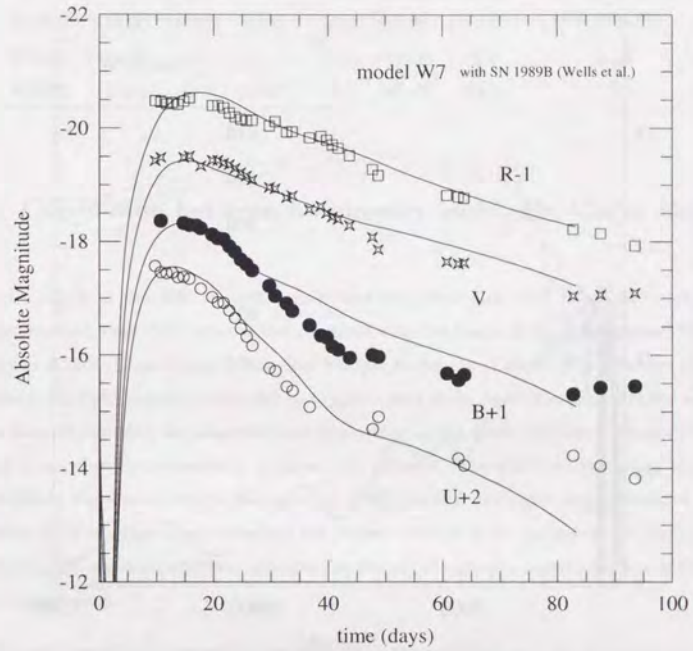


Figure 5.3: Monochromatic light curves of model W7. $U+2, B+1, V, R-1$ are plotted with the observation of SN 1989B (Wells et al. 1994).

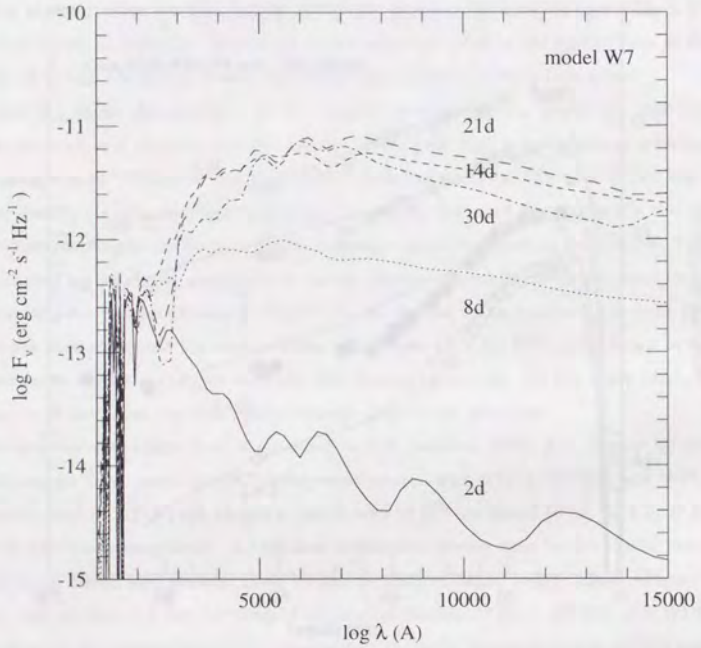


Figure 5.4: Evolution of the emergent spectrum of W7. Plotted are spectra at different phases: 2, 8, 14, 21, and 30 days after explosion.



Table 5.1: Properties of Calculated Light Curve Models

| Models | $M_{\rm bol}$ (mag) | $t_{M\rm bol}$ (day) | $B_{\rm max}$ (mag) | $t_{B\rm max}$ (day) | $V_{\rm max}$ (mag) | $t_{V\rm max}$ (day) | $(B-V)_{V\rm max}$ | $\Delta M_{15}(B)$ (mag) |
|---|---|---|---|---|---|---|---|---|
| W7 | -19.0 | 12 | -18.6 | 14 | -18.92 | 14 | 0.32 | 1.1 |
| W7DT | -19.57 | 11 | -19.05 | 7 | -19.61 | 11.4 | 0.4 | 0.95 |
| W7DN | -19.68 | 11 | -19.10 | 7.6 | -19.74 | 12 | 0.8 | 0.64 |
| W7DHE | -19.56 | 11 | -18.94 | 9.5 | -19.90 | 11.6 | 0.97 | 0.81 |
| WDD1 | -18.66 | 14.7 | -18.35 | 13.3 | -18.86 | 14.7 | 0.53 | 1.53 |
| WDD2 | -19.55 | 11.1 | -19.18 | 12.1 | -19.40 | 12.7 | 0.22 | 0.82 |
| WDD3 | -19.55 | 10.9 | -19.27 | 10.9 | -19.47 | 12.1 | 0.2 | 0.93 |

## 5.4 Correlation between Luminosity and Light Curve Shape

Recent analysis of the SNe Ia light curves have suggested that SNe Ia are not quite standard candles, instead, that their luminosities correlate with the shape of the light curves(Phillips 1993; Hamuy *et al.*1995; Riess, Press, & Kirshner 1995ab; Hamuy *et al.*1996). The observed trend is that slow declining light curves correspond to brighter, and faster light curves to dimmer supernovae. It has been shown that the observational dispersions in the peak absolute magnitudes of SNe Ia largely drop when this correlation is taken into account. The observed sample of 13 SNe Ia by Cálan Tololo Supernova Search(Hamuy et al. 1995) showed that there are as much as $\sim 0.5$ mag spread in the $V$ absolute magnitude and the decline rates lie in the range of $0.8 < \Delta m_{15}(B) < 1.5$. Here $\Delta m_{15}(B)$ is a quantity that measures the drop in $B$ apparent magnitude during first 15 days after its maximum.

We find some slight correlations between the peak magnitude and the decline rate in the same sense as in the observations. In the upper panel of Figure 5.15, we plotted the maximum $V$ magnitude against $\Delta M_{15}(B)$ for all the calculated models in the present study. The dotted line shows the observed tendency on the same diagram derived by Hamuy et al.(1996), which has approximately an inclination of $\sim 0.7$. This is also in agreement with the result by Phillips(1993) (Figure 1.3 in Chaper 1), though his sample is smaller than that of Hamuy et al.(1996) and his plot shows steeper inclination. Our result clearly indicates that despite the small number of theoretical models in our sample the observaed spread and correlations of peak magnitude and decline rate can be explained within the Chandrasekhar mass models.

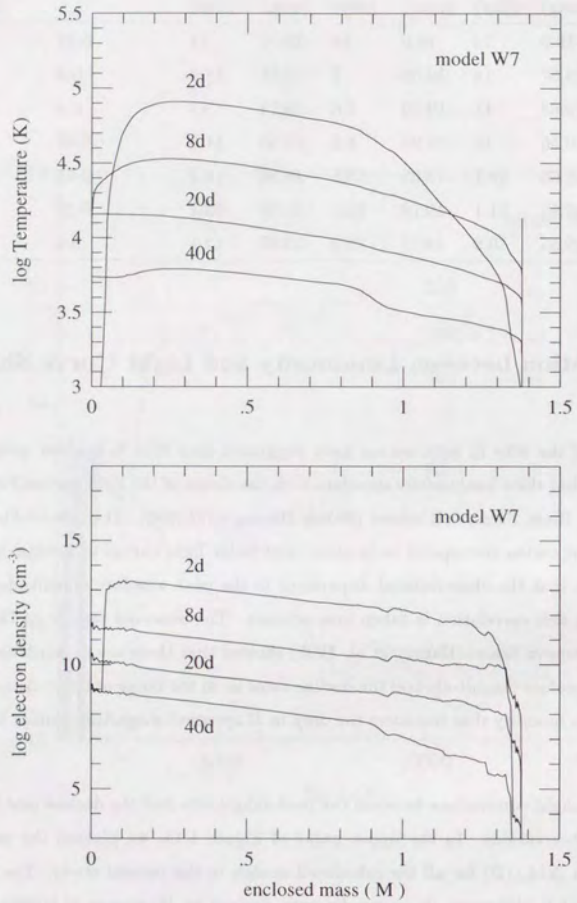


Figure 5.5: Changes in the distributions of temperature and electron density in model W7 (2, 8, 20, and 40 days after explosion)



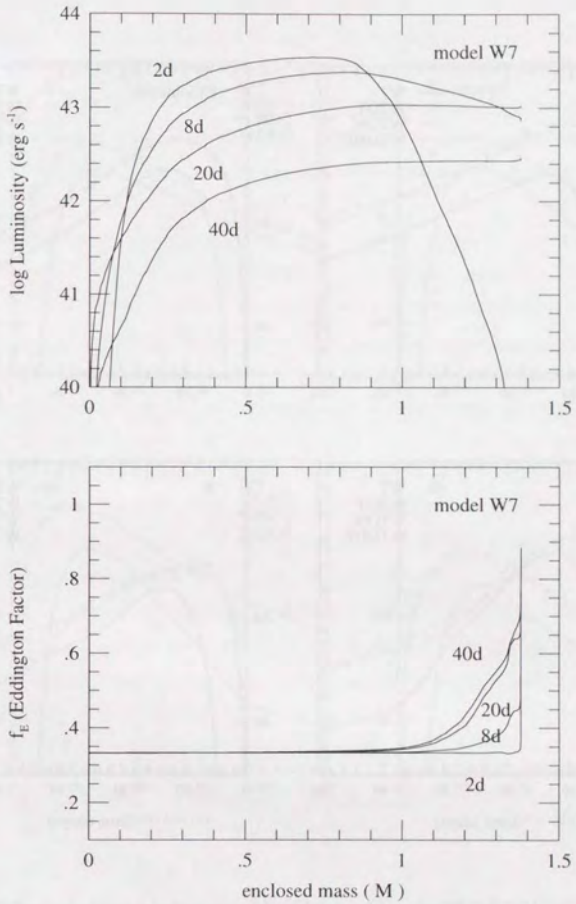


Figure 5.6: Time evolution in the (inertial frame) luminosity and the Eddington factor in the case of W7.

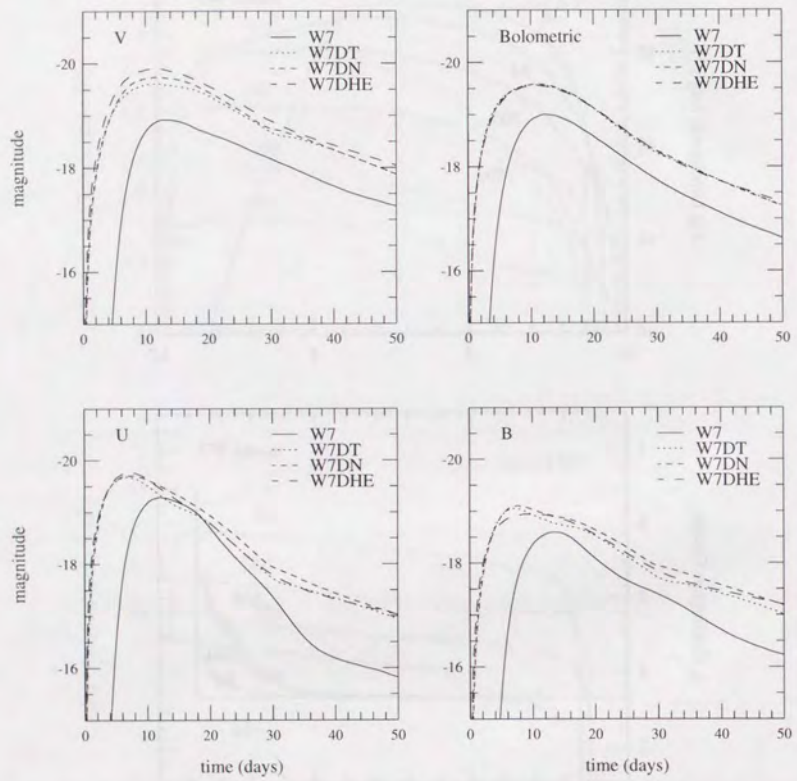


Figure 5.7: Bolometric and $UBV$ monochromatic light curves for deflagration model(W7) and late detonation models(W7DT, W7DN, W7DHE).



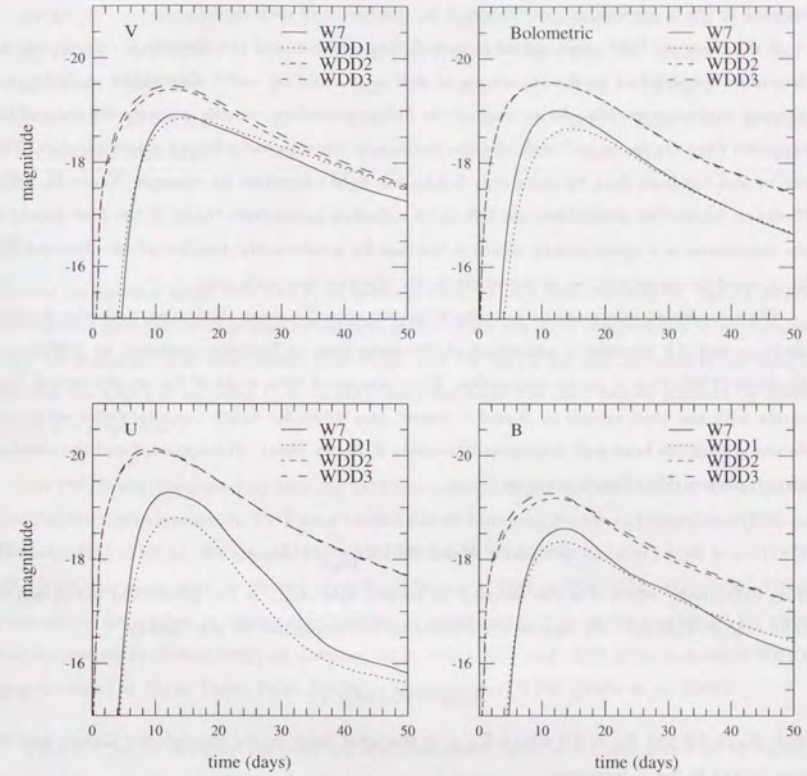


Figure 5.8: Same as Figure 5.7 but for delayed detonation models(WDD1, WDD2, WDD3). Also shown is the light curves for W7 for comparison.

## 5.5 Comparisons with Observations

In this section, we compare our theoretical light curves with some of the well observed nearby SNe Ia and determine the distances to them. Although the number of the adopted models is limited, they encompasses a wide range of different explosion models that are currently considered to be relevant to SN Ia explosions (see chapter 2 for the details of each model).

If the observed light curve agrees in overall shape with one of the theoretical models, we can determine the distance to the supernova as well as it could be useful diagnostics to distinguish different explosion models. As a result of the fitting procedure, we can estimate the time of the explosion from the horizontal shift and the distance to the supernova from the vertical shift. This can be and has been done by using only bolometric light curves(see for example, Yamaoka 1992). However, interstellar extinctions are left to be unknown parameters there. If the host galaxy of the supernovae is a spiral galaxy, which is the case for a substantial fraction of the observed SNe Ia, it could be major sources of the errors in the distance determination.

With combined informations in more than two colors, we can determine both the distance modulus and the interstellar extinction at the same time as first demonstrated by Höflich and Khokhlov(1993) that it works in practice. They compared their state of the art theoretical light curves with the observations in $B$ and $V$ bands, two colors for which the interstellar extinction for our galaxy has been well determined(Burstein & Heiles 1984). The apparent and the absolute magnitude are related each other as

$$m_{\rm color} - M_{\rm color} = 5\log\frac{d}{10{\rm pc}} + A_{\rm color}, \tag{5.21}$$

from definitions, where $d$ is the distance in parsecs and $A_{\rm color}$ is the interstellar extinction for color $= U, B, V, R,$ or $I$. We assume the interstellar reddening law for our Galaxy

$$A_{\rm color} = R_{\rm color} E_{B-V}, \tag{5.22}$$

with $R_B = 3.0$ and $R_V = 4.0$ where $E_{B-V}$ is the total color excess through our Galaxy and the host galaxy of the supernovae,

$$E_{B-V} = E_{B-V,{\rm Galactic}} + E_{B-V,{\rm host}}. \tag{5.23}$$

We use the Galactic values from Burstein & Heiles(1984) and the intrinsic color excess $E_{B-V,{\rm host}}$ is obtained as a result of light curve fitting.

Table 5.2 lists a sample of the observed nearby SNe Ia for which we try to seach for a possible theoretical model. Accurate CCD photometries have been taken and published for the latest three SNe Ia in table 5.2. These are also the supernovae after the subclass Ia has been established. We



Table 5.2: List of the Observed SNe Ia Compared to our Models

| Supernova | Parent galaxy | (Type) | $cz$ (km s$^{-1}$) | $m-M$ (mag) | $E_{B-V}$ | Distance (Mpc) | Best Fit Model |
|---|---|---|---|---|---|---|---|
| SN 1937C | IC4182 | Sm | 326 | $27.7 \pm 0.3$ | $0.04 \pm 0.07$ | $3.47 \pm 0.4$ | W7 |
| SN 1972E | NGC5253 | I | 407 | 27.6 | 0.03a | $3.3 \pm 0.3$ | W7 |
| SN 1981B | NGC4536 | Sb | 1647 | $31.7 \pm 0.3$ | $0.04 \pm 0.07$ | $14 \pm 2$ | W7 |
| SN 1989B | NGC3627 | Sb | 726 | 30.6 | 0.3b | $13.2 \pm 3$ | W7 |
| SN 1991T | NGC4527 | Sb | 1727 | 30.5 | 0.13 | $12.6 \pm 2$ | W7DT |
| SN 1994D | NGC4526 | S0 | 487 | 31.0 | 0.0 | $15.8 \pm 2$ | W7 |

include the peculiar event SNe 1991T, an extreme event of over-luminous SNe Ia, and SN 1994D, a somewhat peculiar event among recent SNe Ia for which the most complete set of photometric data are available. The older events SNe 1937C and SN 1972E are also included in our sample, because the Cepheid variables have recently been discovered in their parent galaxies by *Hubble Space Telescope(HST)*

SN 1972E was discovered on May 15, 1972 in an irregular galaxy NGC 5253 by Kowal(1972). The followup photometries in *UBV* were carried out at European Southern Observatory(ESO) on Cerro La Silla in Chile. We adopted the tabulated data published by Ardeberg & de Groot(1973). SN 1981B was discovered by Tsvetkov(1981) on March 2, 1981 in NGC4536. We use the UBVR photometric data taken at McDonald Observatory published in Buta & Turner(1983). SN 1989B was discovered by Evans(1989) on January 30 in NGC 3627 and CCD photometries in UBVRI were obtained at Cerro Tololo Inter-American Observatory(CTIO) (Wells et al. 1989).

Figures 5.9-5.14 compare the observed and theoretical light curves that give best fit amoung the models we surveyed. Although the accuracy of fitting is different from event to event, we confirmed that all the events in Table 5.2, except for SN 1991T, are basically in good agreement with a standard deflagration model W7 in overall shape. Obviously, SN 1991T requires a different model that could explain its broad peak and much slower decline. We found that a late detonation model W7DT can reproduce the whole light curve shape of SN 1991T. This is expected from the fact that W7DT is a model proposed by Yamaoka et al. (1992) to explain the bolometric light curve and expansion velocity of SN 1991T. The feasibility of W7DT as a model for SN 1991T is reinforced by our comparison of monochromatic light curves.

## 5.6 Comparative Distance Determinations

There have been developed so far various kinds of methods for determination of the extragalactic distances: Cepheid variables, the Tully-Fisher relation, the $D_n - \sigma$ relation, Surface Brightness Fluctuations, Brightest Cluster Galaxies, and Type Ia Supernovae.(see a recent review by Willick 1996). The distances to the host galaxies of nearby supernovae have been mainly determined by the Tully-Fisher(TF) method or Surface Brightness fluctuation(SBF) method. However, after the HST Cepheid Project was launched, many Cepheid variables have been discovered in nearby galaxies. It is tempting for us to compare our distance estimates to those Cepheid distances if available.

In Table 5.2, we give the distance modulus and the diatance in Mpc for indivisual SN Ia using the theoretical model in the last column, by applying the fitting procedure described in the previous section. The errors in the distance estimate include the uncertainties in the color excess $E_{B-V}$ we found in the literatures, but a possible uncertainty inherent in model prediction are not taken into account. For SNe 1937C, 1972E, a number of Cepheid variables have been discovered through the HST Cepheid Project and the distances to their parent galaxies have been newly determined using the well established period-luminosity relation.

The distance to Sdm galaxy IC 4182, the host galaxy of SN 1937C, were derived to be $28.36 \pm 0.09$ mag from 28 Cepheids. Similarly, the distances to 1972E are given by Sandage et al.(1994), which yielded a distance modulus of $28.06 \pm 0.06$ mag. Our estimate gave smaller values than these Cepheid distances for both two SNe Ia. Nomoto et al.(1996) discussed the case of SN 1937C. They argue that if we adopt the Cepheid distance to IC 4182 determined by HST observation and take a reasonable range of the value of $H_0$, SN 1937C would be somewhat brighter than typical SNe Ia. Our estimate also shows that SN 1937C might be a little bit brighter than normal SNe Ia, though our model prediction of peak luminosity tends to be lower than the average of the observed SNe Ia.

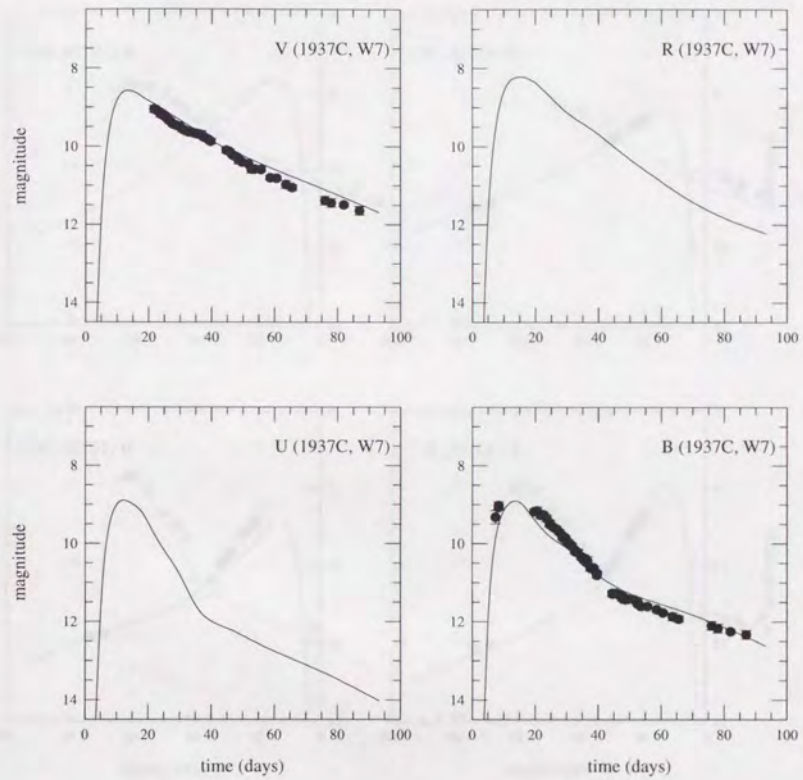


Figure 5.9: Monochromatic light curves of SN 1937C with theoretical light curves of W7.

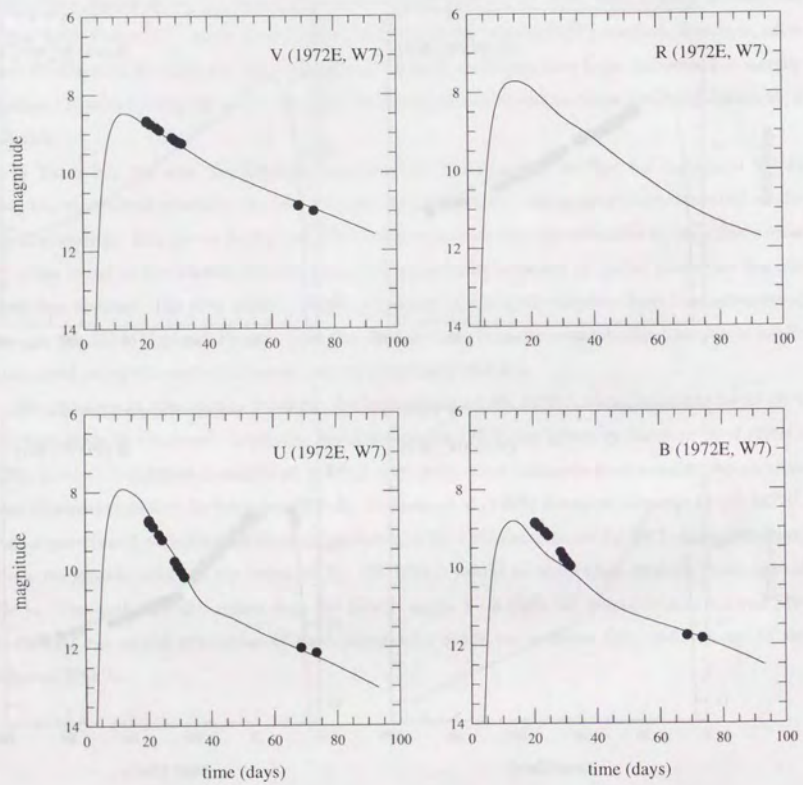


Figure 5.10: Monochromatic light curves of SN 1972E with theoretical light curves of W7.



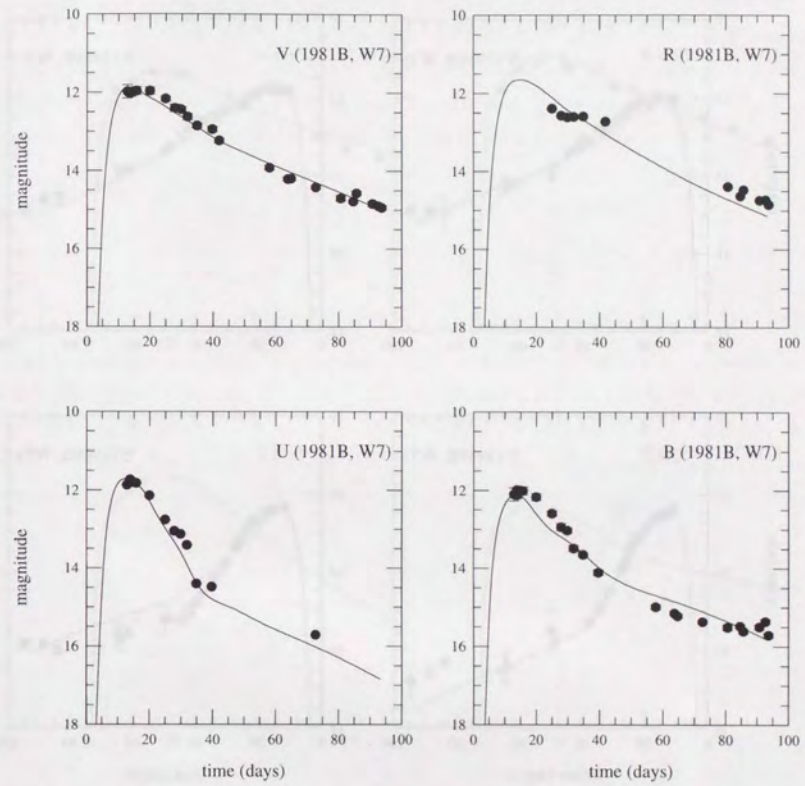


Figure 5.11: Monochromatic light curves of SN 1981B with theoretical light curves of W7.

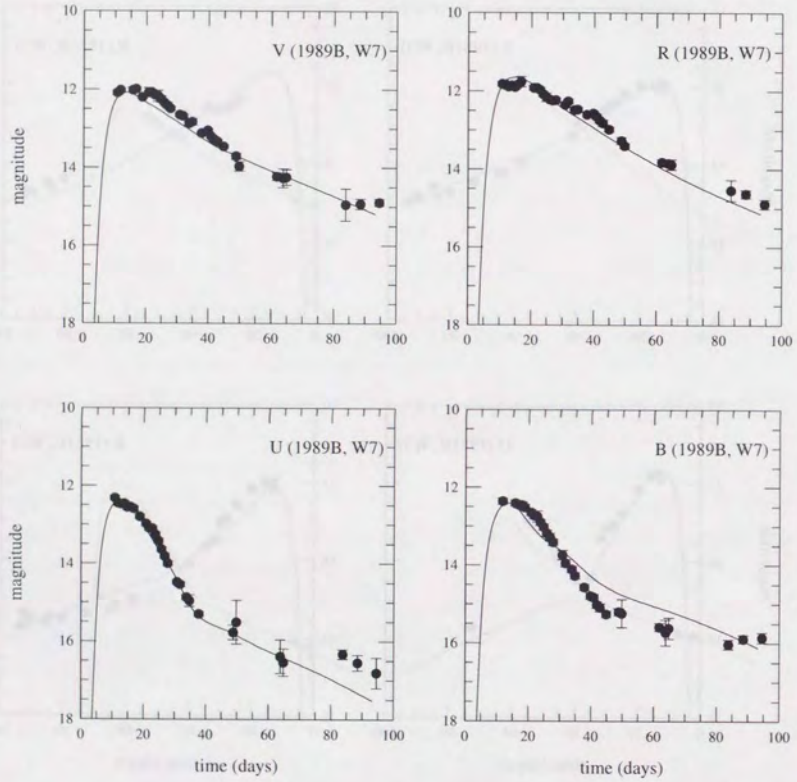


Figure 5.12: Monochromatic light curves of SN 1989B with theoretical light curves of W7.



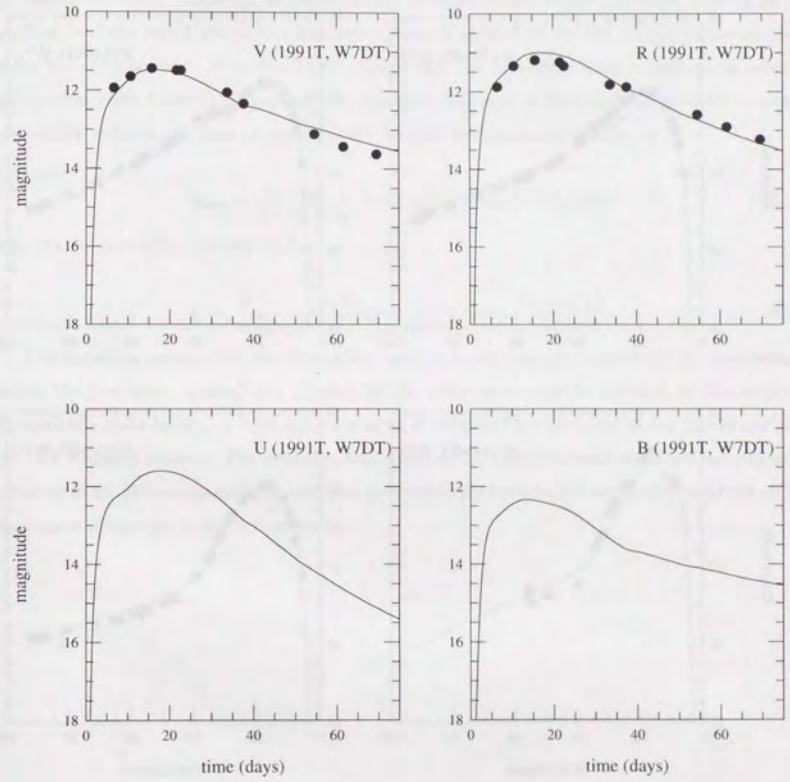


Figure 5.13: Monochromatic light curves of SN 1991T with theoretical light curves of W7DT.

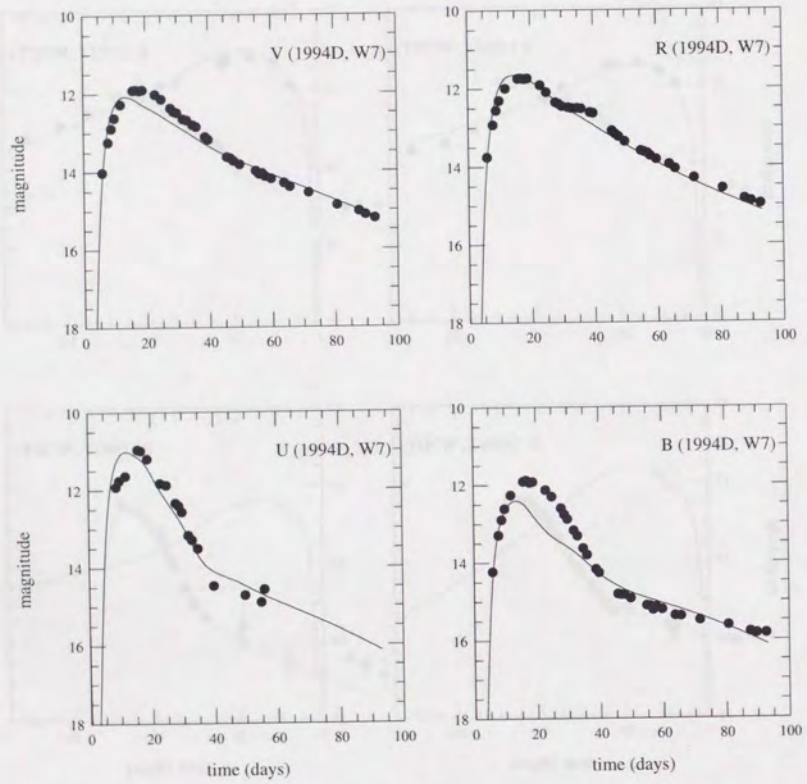


Figure 5.14: Monochromatic light curves of SN 1994D with theoretical light curves of W7.



## 5.7 Expansion Effect on Line Opacity

The effects of expansion on the line contributions to the mean opacities are important for quantitative predictions of supernovae light curves. Karp(1976) studied the line contributions to the Rosseland mean opacity in expanding medium and demonstrated that it is significantly enhanced by expansion effect. Recently, Blinnikov(1995) formulated the Rosseland mean opacity in expanding medium based not on the heuristic approach applied so far but on the formal solution of the radiative transfer. Blinnikov(1995) showed that the redshifted lines contribute to enhance the opacity while Karp(1976) assumed its opposite. Eastman & Pinto(1993) applied the escape probability method and gave an approximate formula for expansion opacity as

$$\chi_{\rm exp} = \frac{\nu}{\Delta\nu}\frac{v}{rc}\Sigma_j \int_0^1 (1+Q\mu^2)(1-\exp[-\tau_j(\mu)])d\mu \tag{5.24}$$

with the Sobolev optical depth $\tau_j(\mu)$

$$\tau_j = \frac{h}{4\pi}\frac{n_l B_{lu}}{(\partial v/\partial r)(1+Q\mu^2)/c}\left(1-\exp\left(-\frac{h\nu_j}{k_B T}\right)\right). \tag{5.25}$$

This equation means that the expansion opacity is the average number of line interactions within the frequency interval $\Delta\nu$, divided by the distance $\sim ct\Delta\nu/\nu$ traveled by the photons. For optically thick lines $\chi_{\rm exp}$ does not depend on density and proportional to the number of lines per unit frequncy interval. For optically, thin lines, $chi_{\rm exp}$ coincides with the usual opacity as in equation (5.9). We are planning to examine quantitatively the effect of expansion opacities on the light curve properties in the future study.

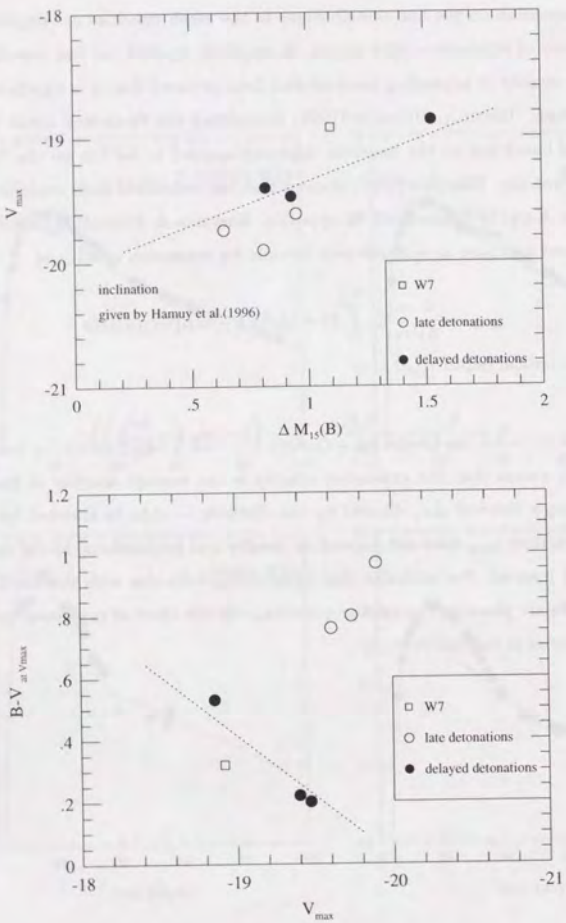


Figure 5.15: Calculated light curve properties: (1) correlation between maximum $V$ magnitude and $\Delta M_{15}(B)$ (upper panel) and (2) $V$ versus $B-V$ color at $V$ maximum (lower panel).

# Chapter 6

# Determinations of Cosmological Parameters

## 6.1 Overview

The Hubble constant $H_0$ is one of the most important parameter in observational cosmology, which affects the age and size of the universe. There have been developed various kinds of methods to measure $H_0$ by observations: the use of the Tully-Fisher(T-F) relation, the Surface Brightness Fluctuations(SBF), and the planetary nebulae luminosity function(Jacoby et al. 1990), a method based on the Sunyaev-Zel'dovich effect, and the use of Type Ia supernovae. To survey all the methods and the values obtained in indivisual estimates is not only beyond the scope of this study but also not likely to bring no fruitful results in the present status. We just intend to apply our results in the distance determinations to give a tentative estimate for $H_0$.

Recently, the Calán/Tololo supernova survey(Hamuy et al. 1995) has discovered $\sim$ 30 SNe Ia at redshifts out to $z \sim 0.1$, which provided well observed high quality sample of intermediate redshift SNe Ia. The discovery of high redshift SNe Ia 1988U at $z = 0.31$ (Norgaard-Nielsen et al. 1989) tempted us to apply it for a determination of other cosmological parameters such as $q_0$ and $\Omega_0$. Perlmutter et al.(1995) reported the discovery of SN Ia 1992bi at $z = 0.458$ and gave a estimate of $q_0$ assuming the absolute magnitude of normal SNe Ia.

It has been considered until recently that SNe Ia are homogeneous in their luminosities enough to be regarded as "standard candles". Branch & Miller(1993) studied the distribution of the blue absolute magnitudes of SNe Ia with the distances determined by the Tully-Fisher(TF) or $D_n - \sigma$ techniques. They derived a mean maximum absolute magnitude $M_B = 19.72 \pm 0.06 + 5\log(H_0/50)$ with an observational dispersion of only $\sigma(M_B) = 0.36$, which is comparable to the combined errors in distance, apparent magnitude, and extinction. Sandage & Tammann(1993) derived the

Hubble constant from the Cepheid distance calibration in V band for IC 4182(SN 1937C) d by *Hubble Space Telescope(HST)*. They argued that most of the observed dispersions is due to the observational errors rather than being intrinsic if we use the slope of the Hubble diagram expected from the linear redshift-distance relation.

After the discovery of peculiar SNe Ia and the significant dispersions in the light curve properties, two major elaborate methods for determination of $H_0$ have been developed by several authors. One is a purely empirical approach based on the careful statistical analysis of the light curve shape. Riess, Press, & Kirshner (1995a) developed the light curve shape(LCS) method to estimate the luminosity of SNe Ia by using whole information on the light curve shapes. They made a "training set" of light curves for supernovae in galaxies whose relative distances have been accurately measured. They obtained $H_0 = 64 \pm 3$ fixing the absolute distances with three Cepheid-calibrated SNe Ia. With the luminosity-decline rate correlation taken into account, Hamuy et al.(1996) could obtained a Hubble diagram with less dispersion for the sample discovered by the recent Calán/Tololo supernova survey, yielding the value of $H_0 = 63.1 \pm 3.4$. Another method is based on the detailed theoretical predictions of the light curve shape using a complete set of the currently plausible explosion models. Höflich & Khokhlov(1996) compare observed light curves with their state of the art theoretical light curves and gave their estimates of $H_0$ for 26 SNe Ia. By averaging the values from indivisual estimates, they conclude that $H_0 = 67 \pm 9$ at 95 % confidence level.

## 6.2 Hubble Constant

Based on our theoretical light curves, we try to estimate the value of the Hubble constant for all nearby SNe Ia listed in Table 5.2 and four additional SNe Ia at higher redshifts $z \sim 0.1 - 0.5$ (Hamuy et al. 1996; Perlmutter et al. 1995) in Table 6.1. In order to take into account the corrections due to the redshift effects, we first describe the formulation that is applicable to high redshift cases. From definition, the distance modulus is

$$m - M = 25 + 5\log_{10} d_L, \tag{6.1}$$

where $d_L$ is the luminosity distance in Mpc. In a Robertson-Walker universe with the cosmological constant $\Lambda = 0$, the luminosity distance $d_L$ depends on the Hubble constant $H_0$ and the deceleration parameter $q_0$ as

$$d_L = \frac{c}{H_0}\left(z + \frac{1}{2}(1 - q_0)z^2 + O(z^3)\right). \tag{6.2}$$

or equivalently, using distance modulus, we have an approximate formula correct for small $z$ ,



Table 6.1: High Redshift SNe Ia Used in our Estimate of Cosmological Constants

| Supernova | Parent galaxy | (Type) | redshift ($z$) | $m - M$ (mag) | Fitted Model |
|---|---|---|---|---|---|
| SN 1988U | NGC4526 | S0 | 0.31 | 40.8 | W7 |
| SN 1992aq | anonymous | Sa? | 0.1018 | 38 | W7 |
| SN 1992bi | anonymous | ? | 0.458 | 40.7 | W7 |
| SN 1992br | anonymous | E0 | 0.0882 | 38.3 | W7 |

$$m - M = 25 - 5\log_{10} H_0 + 5\log_{10} cz + 1.086(1 - q_0)z + O(z^2). \tag{6.3}$$

where $H_0$ and $cz$ are in km s$^{-1}$ Mpc$^{-1}$ and km s$^{-1}$, respectively(Weinberg, 1972; Kodama 1988). In the limit of $z \to 0$, equation (6.2) reduces to the usual Hubble relation,

$$d = \frac{cz}{H_0}. \tag{6.4}$$

In order to measure $q_0$, distant supernovae at $z > 0.1$ are needed. Note, however, that all the needed information to determine $q_0$ is a relation of $m$ versus $z$ and the value of $H_0$ is not required.

To make comparison between the observed and theoretical light curves, we have also take into account the change in the spectra during light propagation in the Universe. This can be done by using so called "K-correction" term(Oke & Sandage 1968). However, we can calculate directly the observed spectra at an arbitrary cosmological redshift, since we have the monochromatic light curves. If the supernova at redshift $z$ has an intrinsic spectrum $F_\lambda(t)$, the observed magnitudes at dilated time $t' = t(1+z)$ are

$$M_{\rm color}(t') = -2.5\log\left\{\frac{1}{1+z}\int_0^\infty F_{\frac{\lambda'}{1+z}}(t)T_{\rm color}(\lambda')d\lambda'\right\} + \text{const.} \tag{6.5}$$

where $F_\lambda$ is the intrinsic monochromatic flux of the supernova and $T_{\rm color}(\lambda)$ is the transmission function of each photometric band. The observed spectrum is redshifted by a factor of $(1+z)$ due to the expansion of the Universe and is weakened by a factor of $(1+z)$ because of time dilation. Figure 6.1. illustrates the effets of the cosmological redshift on the shape of monochromatic light curves in the case of W7. It is seen that the effects are different at different phases because of the change in the the spectrum.

Figures 6.2 and 6.3 compare the light curves of four distant SNe Ia in Table 6.1 with the theoretical monochromatic light curves for W7 at the corresponding redshifts. We also list the

obtained distance modulus in Table 6.1. For SN 1988U, Norgaard-Nielsen et al.(1989) gave an estimate of $m - M = 40.10 - 39.97$ for $q_0 = 0.1 - 0.5$.

In Figure 6.4, we draw a Hubble diagram using all the SNe Ia for which we determined their distances. The distance moduli are plotted against $\log_{10}(cz)$. The two dotted lines indicate the cases for $H_0 = 50$, and 100 km s$^{-1}$ Mpc$^{-1}$, respectively. The values of the Hubble constant obtained from light curve fits to each SNe Ia show a wide spread between $H_0 = 50 - 100$. Because of the small number of the observation points, the fitting to the theoretical light curves can not be free from a significant ambiguity, especially for distant SNe Ia, and even for some of the nearby SNe Ia. The uncertainty in the interstellar reddening could produce an error in the distance modulus as much as $\sim 0.3$ mag. Moreover, it is difficult to separate the contribution of the peculiar velocity field from the observed recession velocities for nearby sample.

We tried to estimate the Hubble constant using the three relatively distant SNe Ia 1992br, 1992aq, and 1988U, for which we succeeded to get good fits to theoretical light curve models. The results are $H_0 = 58$, 77, and 64 km s$^{-1}$ Mpc$^{-1}$, respectively. Therefore, we can tentatively conclude $H_0 = 66 \pm 12$ km s$^{-1}$ Mpc$^{-1}$. This value is compatible with the values derived by Höflich & Khokhlov(1996) or Riess, Press, & Kirshner(1995).

Finally, we try to derive a value of $q_0$ by simply fitting the most distant four SNe Ia in our sample to equation (6.3). The best fit with least minimum quare gives $H_0 = 58.6$ and $q_0 = 2.84$ as is shown in Figure 6.5. Our result strongly suggests a positive value of $q_0$. It should be noted, however, that this estimate is based on the assumption of $\Lambda = 0$ so that it is too restrictive to draw any firm conclusion for the value of $q_0$. In addition, concerning the errors in the interstellar reddening and the photometries and also the uncertainties arising from fitting procedure, it is premature, in our present study, to give some conclusive predictions for the values of $H_0$ and $q_0$.



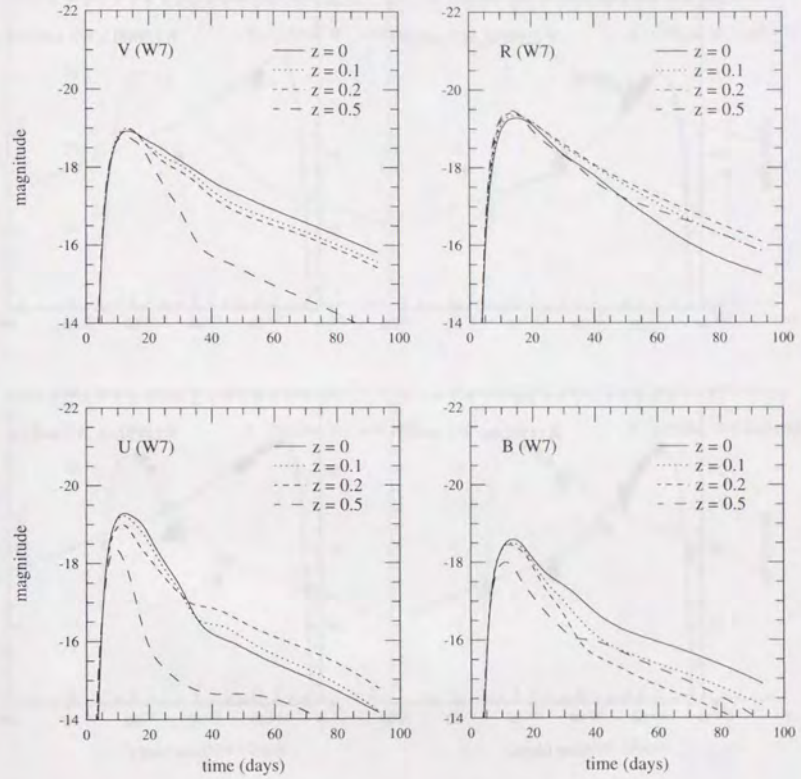


Figure 6.1: Monochromatic light curves of W7 model at different cosmological redshifts.

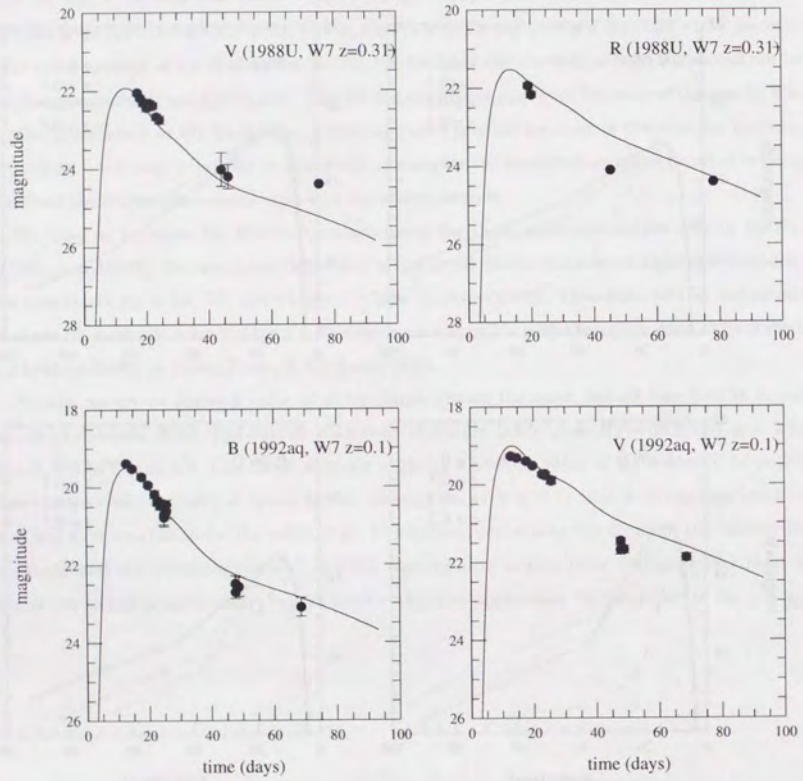


Figure 6.2: Monochromatic light curves of SN 1988U and SN 1992aq with W7 at cosmological redshifts $z = 0.31$ and 0.10, respectively.



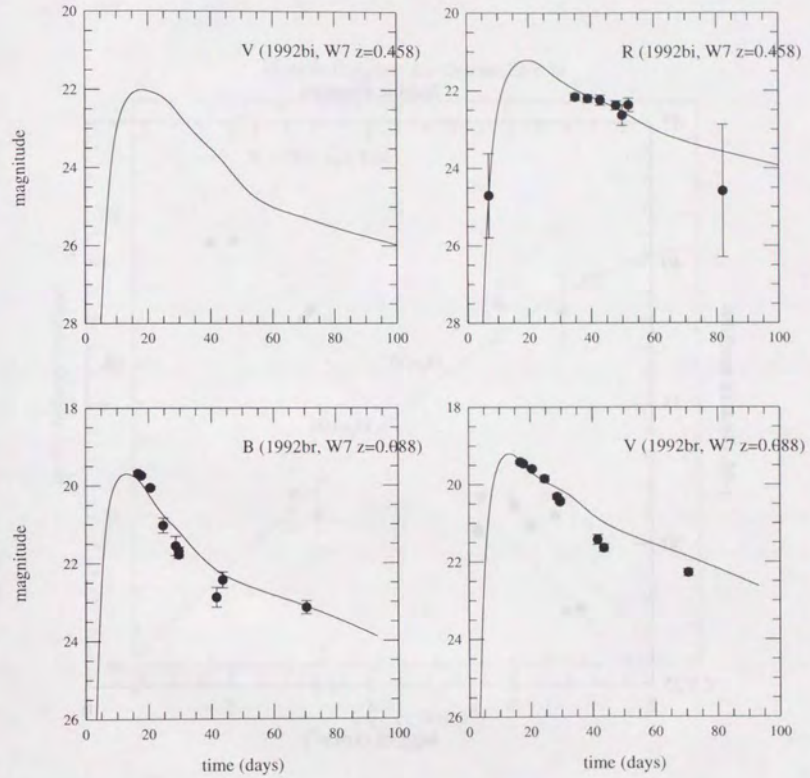


Figure 6.3: Monochromatic light curves of SN 1992bi and SN 1992br with W7 at cosmological redshifts $z = 0.458$ and 0.088, respectively.

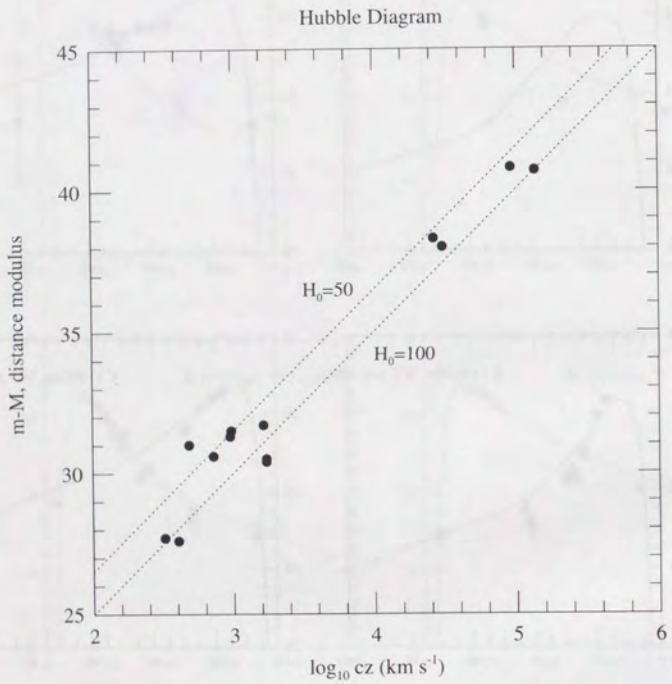


Figure 6.4: Hubble diagram with all SNe Ia in our sample. The distance modulus are plotted against cz(km $s^{-1}$.



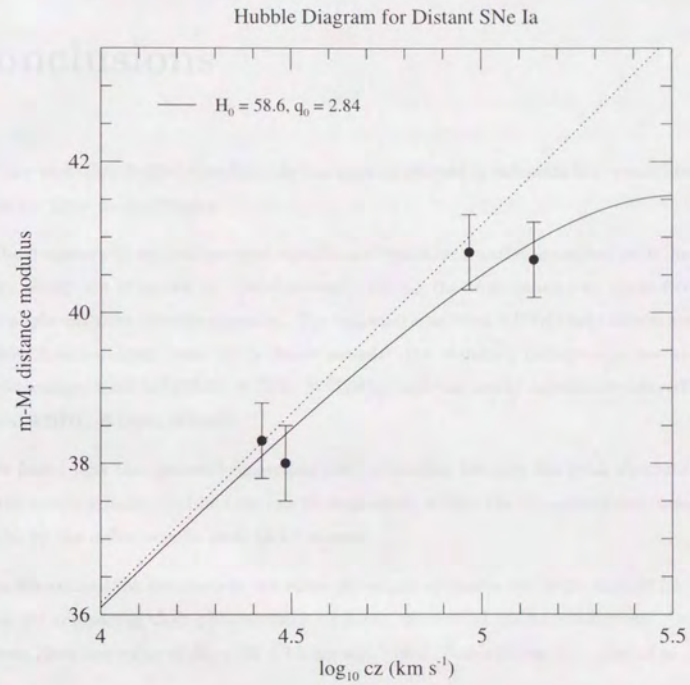


Figure 6.5: Same as Fig.6.4 but with only distant SNe Ia ($z \geq 0.1$). The solid curve shows the best fit of equation (6.3) to the observations, which is obtained by $H_0 = 58.6$, and $q_0 = 2.84$. The plotted error bars in distance moduli indicate 0.5 mag dispersions.

# Chapter 7

# Conclusions

1. A new radiation hydrodynamics code has been developed to calculate the monochromatic light curves for Type Ia supernovae.

The frequency integrated moment equations of radiative transfer are solved with the Eddington factors which are obtained by simultaneously solving the time-dependent multi-frequency and multi-angle radiative transfer equation. The bolometric and the *UBVRI* light curves are calculated for the Chandrasekhar mass white dwarf models: the standard deflagration model (W7), the late detonation models(W7DT, W7DN, W7DHE), and the newly calculated delayed detonation models(WDD1, WDD2, WDD3).

2. We found that the observed dispersion and correlation between the peak absolute magnitude and the postmaximum decline rate can be explained, within the Chandrasekhar mass explosion models, by the differences in their nickel masses.

3. We determined the distances to the observed sample of nearby and high-redshift ( $z \sim 0.1-0.5$) SNe Ia by comparing their photometries with our theoretical model predictions. Our tentative estimate gives the value of $H_0 = 66 \pm 12$ km sec$^{-1}$ Mpc$^{-1}$ and favors the value of $q_0 \geq 1$.

## Acknowledgement

I would like to express my deep appreciation to my supervisor Prof. Ken'ichi Nomoto for introducing me into a fantastic field in astrophysics, supernovae and related phenomenon. Without his invaluable advice and continuous encouragement, I could not have completed this work. I'd like to express my gratitude to Prof. Serguei Blinnikov and Dr. Peter Höflich. To go through with this work, I owed much to invaluable discussions with them on the matters of radiative transfer and opacities. I would like to express my special gratitude to Drs. Toshikazu Shigeyama, Timothy Young, Shiomi Kumagai, Tomoharu Suzuki, and Kazuhiro Shimasaku for useful discussions and practical helps during the past several years. I would also like to thank Drs. Izumi Hachisu and Hideyuki Saio for their kind helps and useful discussions. I'd like to thank Prof. Takashi Tsuji and Dr.Keiichi Ohnaka for kindly providing me their machine readable files for atomic data. Finally, I would like to express my deep gratitudes to my parents, grandparents and my younger sister from the bottom of my heart. They have constantly helped and encouraged me for long years. Some part of the computations in this work were carried out on the Fujitsu-VPP500 system at Institute of Astronautical Science(ISAS) and at Institude of Physical and Chemical Research(RIKEN), and on the VPP300 system at National Astronomical Observatory(NAO in Mitaka, Tokyo). This work has been supported in part by the fellowship of the Japan Society for Promotion of Science(JSPS) for Japanese Junior Scientists(4227).

# References

Ardeberg A., & de Groot M., 1973, A&A, 28, 295

Arnett W.D., 1969, Ap&Sp, 5, 180

Arnett W.D., 1982, ApJ, 253, 785

Arnett W.D., & Livne E., 1994, ApJ, 427, 314

Burstein D., & Heiles C., 1984, ApJS, 54, 33

Bartunov O.S., Blinnikov S.I., Pavlyuk N.N., Tsvetkov D.Yu., 1994, A&A, 281, L53

Blinnikov S.I., & Bartunov O.S., 1993, A&A, 273, 106

Blinnikov S.I., 1995, MPA Green Report 913, to be published in the proceedings of NATO ASI Conference "Thermonuclear Supernovae"

Blinnikov S.I., 1996, Pis'ma v AZh, 22, 92(Astron.Letters. J.Astron.Space Sci. 22, 79)

Boffi F., & Branch D., 1995, PASP, 107, 347

Branch D., Doggett J.B., Nomoto K., & Thielemann F.-K., 1985, ApJ, 294, 619

Branch D., Nomoto K., & Filippenko A.V., 1991, Comments on Astrophysics XV, 221

Branch D., Livio M., Yungelson L.R., Boffi F.R., Baron E., 1995, PASP, 107, 1019

Buta R.J., & Turner A., 1983, PASP, 95, 72

Canal R., Ruiz-Lapuente P., & Burkert A., 1996, ApJ, 456, L101

Eastman R., Pinto P., 1993, ApJ, 412, 731

Eastman R., Schmidt B., Kirshner R., 1996, ApJ, 466, 911

Eck C., Cowan J.J., Roberts D.A., Boffi F.R., & Branch D., 1995, ApJ, 451, L53

Evans R.O., 1989, IAU Circ., 4726

Filippenko Kirshner R., 1996, ApJ, 466, 911

Ford C.H., Herbst W., Richmond M.W., Baker M.L, Filippenko A.V., Treffers R.R., Paik Y., & Benson P.J., 1993, AJ, 106, 1101

Hachisu I., Kato M., & Nomoto K., 1996a, in Supersoft X-ray Sources, eds. J.Greiner, J.Truümper, & F.Meyer(Lecture Notes in Physics; Springer-Verlag), in press

Hachisu I., Kato M., & Nomoto K., 1996b, ApJ, 470, L97

Hamuy M., Phillips M.M., Maza J., Suntzeff N.B., Schommer R.A., & Aviles R., 1995, AJ, 109, 1

Hamuy M., Phillips M.M., Suntzeff N.B., Schommer R.A., Maza J., & Aviles R., 1996, preprint

Höflich P.,, & Khokhlov A., 1996, ApJ, 457, 500

Iben I.Jr., & Tutukov A.V., 1984, ApJS, 54, 335

Iben I., Nomoto K., Tornambè A., & Tutukov A., 1987, ApJ, 317, 717

Ivanova L.N., Imshennik V.S., & Chechetkin V.M., 1975, Ap&Sp., 31, 497

Kawai Y., Saio H., & Nomoto K., 1987, ApJ, 315, 229

Kenyon S., Livio M., Mikolajewska J., & Tout C., 1993, ApJ, 407, L81

Khokhlov A.M., 1991a, A&A, 245, 114

Khokhlov A.M., 1991b, A&A, 245, L25

Kowal C.T., 1972, IAU Circ., 2405

Kumagai S., 1989, Ph.D. Thesis, University of Tokyo

Kumagai et al., 1989, ApJ,

Kumagai S., & Nomoto K., 1997, in the proceedings of NATO Advanced Study Institute, "Thermonuclear Supernovae", eds. R.Canal, P.Ruiz-Lapuente, & J.Isern (Kluwer)

Kumagai S., & Nomoto K., 1997

Livio M, & Soker N., 1988, ApJ, 329, 764

Livio M., 1995, in Millisecond Pulsars:A Decade of Surprise, eds. A.Fruchter, M.Tavani & G.Shaviv (Bristol, Institute of Physics Publishing), p.57

Livne E., 1993, ApJ, 406, L17

Livio E., & Arnett D., 1995, ApJ, 452, 62

Lundqvist P., & Cumming R.J., 1996, preprint

Lucy L.B., 1991, ApJ, 383, 308

Mihalas D., 1978, *Stellar Atmosphere*, 2nd ed.(Freeman: San Francisco)

Mihalas D., & Mihalas B.W., 1984, *Foundation of Radiation Hydrodynamics*, (New York: Oxford University Press)

Munari U., & Renzini A., ApJ, 397, L87

Müller E.,& Arnett W.D., 1986, ApJ, 307, 619

Nomoto K., Sugimoto D., & Neo S., 1976, Ap&SS., 39, L37

Nomoto K., 1982, ApJ, 253, 798

Nomoto K., 1982, ApJ, 257, 780

Nomoto K., Thielemann F., & Yokoi K., 1984, ApJ, 286, 644

Nomoto K., & Kondo Y., 1991, ApJ, 367, L19

Nomoto K., Suzuki T., Shigeyama T., Kumagai S., Yamaoka H., & Saio H., 1993, Nature, 364, 507



Nomoto K., Iwamoto K., Nakasato N., Thielemann F.-K., Brachwitz F., Young T.R., Shigeyama T., Tsujimoto T., & Yoshii Y., 1996a, in the Proceedings of NATO Advanced Study Institute, "Thermonuclear Supernovae" eds. R.Canal, P.Ruiz-Lapuente, & J.Isern(Kluwer), p.349.

Nomoto K., Iwamoto K., Young T.R., Nakasato N., & Suzuki T., 1996b, in the Proceedings of NATO Advanced Study Institute, "Thermonuclear Supernovae" eds. R.Canal, P.Ruiz-Lapuente, & J.Isern(Kluwer), p.839.

Norgaard-Nielsen H.U., Hansen L., Henning E.J., Salamanca A.A., Ellis R.S., & Warrick J.C., 1989, Nature, 339, 523

Pierce M.J., & Jacoby G.H., 1995, AJ, 110, 2885

Perlmutter S. et al., 1995, ApJ, 440, L41

Podsiadlowski Ph., Hsu J.J.L., Joss P.C., & Ross R.R., 1993, Nature, 364, 509

Rappaport S., Stefano R. & Smith J., 1994, Apj, 426, 692

Renzini A., Ciotti L., D'Ercole A., & Pellegrini S., 1993, ApJ, 419, 52

Ruiz-Lapuente P., Burkert A., & Canal R., 1995, ApJ, 447, L69

Rybicki G.B., & Lightman A.P., 1979, Radiative processes in astrophysics(New York: Wiley)

Saha A., Labhardt L., Schwengeler H., Macchetto F.D., Panagia N., Sandage A., & Tammann G.A., 1994, ApJ, 425, 14

Sandage A., Saha A., Tammann G.A., Labhardt L., Schwengeler H., Panagia N., & Macchetto F.D., 1994, ApJ, 423, L13

Schaefer B.E., 1995, ApJ, 449, L9

Sramek R.A., Weiler K.W., 1990, in Supernovae, ed. A.G.Petschek (New York, Springer), Chapter 4.

Shigeyama T., Nomoto K., Yamaoka H., & Thielemann F.-K., 1992, ApJ, 386, L13

Swartz D.A., Filippenko A.V., Nomoto K., & Wheeler J.C., 1993, ApJ, 411, 313

Taam R.E., & Bodenheimer P., 1989, ApJ, 337, 849

Tsvetkov, 1981, IAU Circ., 3580

Tutukov A.V., & Yungelson L.R., 1994, MNRAS, 268, 871

Van Regemorter H., 1962, ApJ, 136, 906

van den Heuvel, E.P.J., Bhattacharya D., Nomoto K., & Rappaport S.A., 1992, A&A, 262, 97

Verner D.A., Ferland G.J., Korista K.T., & Yakovlev D.G., 1996, ApJ, 465, 487

Wells L.A., et al., 1994, AJ, 108, 2233

Weinberg S., 1972, *Gravitation and Cosmology* (New York: John Wiley & Sons)

Willick J.A., astro-ph/9610200 24 Oct. 1996, to appear in "Formation of Structure in the Universe", eds. A.Dekel & J.Ostriker (Cambridge University Press)

Williams F.A., 1985, Combustion Theory (Menlo Park: Benjamin/Cummings), p.217

Wheeler, J.C., 1990, in Supernovae, Proceeding of the Jerusalem Winter School, vol6 eds. J.C.Wheeler, T.Piran, and S.Weinberg(Singapore: World Scientific), p.1.

Woosley S.E. & Weaver T.A., 1986a, Lecture Notes in Physics, 255, 91

Woosley S.E. & Weaver T.A., 1986b, ARA&A, 24, 205

Woosley S.E. 1990, in Supernovae, ed. Petschek(Springer), p.182

Woosley S.E. & Weaver T.A., 1994, ApJ, 423, 371

Yamaoka H., Ph.D., 1992, Thesis at University of Tokyo

Yamaoka H., Shigeyama T., Nomoto K., & Thielemann F.-K., 1992, ApJ, 393, L55

Yoshii Y., Tsujimoto T., & Nomoto K., 1996, ApJ, 462, 266

# Appendix A

# Numerical Methods

Here the numerical methods for solving the radiation transfer equation and the radiation hydrodynamics equations are described.

## A.1 Radiative Transfer

The transfer equation (3.10) can be rewriten as

$$\frac{1}{c}\frac{DI_\nu}{Dt} + \frac{\partial I}{\partial r} + \frac{1-\mu^2}{r}\frac{\partial I}{\partial \mu} - a_\nu \frac{\partial}{\partial \nu}(\nu I) + 4a_\nu I = \eta - \chi I. \tag{A.1}$$

$$a_\nu = (1-\mu^2)\frac{v}{cr} + \frac{\mu^2}{c}\frac{\partial v}{\partial r}. \tag{A.2}$$

where we simplify the angle derivative terms in equation (3.10). with a relation $v/r = \partial v/\partial r$ which holds in homologous expansion.

$a_\nu$ reduces to $v/cr \sim (ct)^{-1}$.

Instead of using equation (3.19), we directly calculated the observer frame flux as

$$\begin{aligned} F_\nu &= s\pi \int_{-1}^{1} I(\mu,\nu)d\mu \\ &= 2\pi \int_{-1}^{1} \left(\frac{\nu}{\nu_0}\right)^3 I^0(\mu_0,\nu_0)\frac{d\mu}{d\mu_0}d\mu_0 \\ &= 2\pi \int_{-1}^{1} (1+\beta\mu_0) I^0(\mu_0, \frac{\nu}{1+\beta\mu_0})d\mu_0. \end{aligned} \tag{A.3}$$

## A.2 Radiation Hydrodynamics

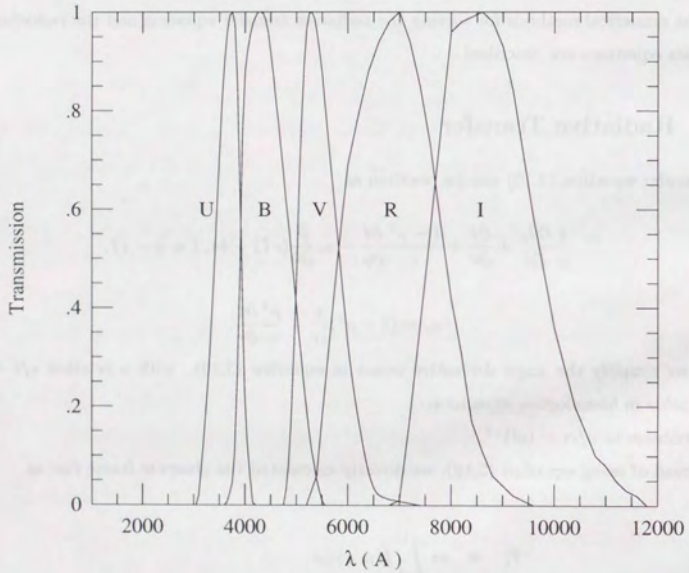


Figure A.1: Transmission functions of $U, B, V, R, I$ photometric bandpasses used to calculate monochromatic light curves(Johnson).